MECHANICAL MICRO-DRILLING OF INCONEL 625 SUPERALLOY USING TUNGSTEN CARBIDE MICRO-DRILL BIT IN DEFORM 3D SOFTWARE

A Thesis
Submitted in partial fulfilment of the
Requirement for the award of the degree of

MASTER OF TECHNOLOGY
IN
MANUFACTURING ENGINEERING
BY

KALYAN KUMAR ADEPU
(20053800006)

Under the supervision of

Dr. ARUNA THAKUR
Assistant Professor

DEPARTMENT OF MECHANICAL
AND
MANUFACTURING ENGINEERING

NATIONAL INSTITUTE OF ADVANCED MANUFACTURING TECHNOLOGY
HATIA RANCHI -834003

2022

TELEPHONE DIRECTOR: 2290859, 2292006
FAX: 0651- 2290860

राष्ट्रीय उन्नत विनिर्माण प्रौद्योगिकी संस्थान
National Institute of Advanced Manufacturing Technology
हटिया, राँची-834 003 (झारखण्ड)
HATIA, RANCHI – 834003 (JHARKHAND)

Ref No…….. Date: ……/……. /2022

DECLARATION CERTIFICATE

This is to be certified that the project report entitled "**MECHANICAL MICRO-DRILLING OF INCONEL 625 SUPERALLOY USING TUNGSTEN CARBIDE MICRO-DRILL BIT IN DEFORM 3D SOFTWARE**" submitted by Kalyan Kumar Adepu (20053800006) in partial fulfilment of the requirement for the award of "Master of Technology in Manufacturing Engineering" of National Institute of Advanced Manufacturing Technology, Hatia, Ranchi is an authentic work carried out under my supervision and guidance. To the best of my knowledge, the content of this thesis does not form a basis for the award of any previous Degree to anyone else.

Date: …

Dr. Aruna Thakur
Assistant Professor
Department of Mechanical and Manufacturing Engineering

Head of Department
Department of Mechanical and Manufacturing Engineering

Dean
(Academic) NIAMT

TELEPHONE DIRECTOR: 2290859, 2292006
FAX: 0651- 2290860

राष्ट्रीय उन्नत विनिर्माण प्रौद्योगिकी संस्थान
National Institute of Advanced Manufacturing Technology
हटिया, राँची-834 003 (झारखण्ड)
HATIA, RANCHI – 834003 (JHARKHAND)

Ref No……... Date: …./……/2022

CERTIFICATE OF APPROVAL

This is to certify the project report entitled "**MECHANICAL MICRO-DRILLING OF INCONEL 625 SUPERALLOY USING TUNGSTEN CARBIDE MICRO-DRILL BIT IN DEFORM 3D SOFTWARE**", is hereby approved as a creditable study of a research topic and has been presented satisfactorily to warrant its acceptance as a prerequisite to the degree for which it has been submitted. It is understood that by this approval, the undersigned does not necessarily endorse any conclusion drawn or opinion expressed therein but approves the thesis for the purpose for which it is submitted.

(Internal Examiner) (External Examiner)

Date: …….
Place: ……

ACKNOWLEDGEMENT

I would like to express my deepest gratitude and admiration to my teacher and guide **Dr. Aruna Thakur**, Assistant Professor, Department of Mechanical and Manufacturing Engineering, NIAMT, Ranchi who is a constant source of guidance, exaltation, and illumination to me. Without her guidance and persistent help, this dissertation would not have been possible.

With a deep sense of belonging, I wish to express my deep sense of gratitude to **Karthik Chandra** research scholar MME Department who helped me at various stages of my project work. I would also like to thank the staff of CCC lab **Himanshu** and **Akash** for their support and help.

Date:

Kalyan Kumar Adepu
M.Tech ME (2020-22)
Manufacturing Department

Place:

ABSTRACT

The Nickel-based superalloys show high strength, and high corrosive resistance even at elevated temperatures. Inconel 625 belongs to the same family of superalloys inheriting the same properties. These properties though making superalloys highly desirable also result in poor machinability. Inconel 625 has very low thermal conductivity causing adiabatic heating during micro-drilling operation which decreases the hardness of the tool. Researchers have tried various methods and techniques to overcome this difficulty arising during micro-drilling but significant results have not been obtained. Performing experiments to try and test various methods and cutting parameters is an expensive endeavour even if we ignore errors and measurement issues that arise during machining. Computer simulations on the other hand provide us with accurate results and measurements to the real world provided correct process models are used. Deform 3D is a powerful process simulation system designed to analyse the three-dimensional (3D) flow of complex manufacturing processes. Various parameters can be easily varied in Deform 3D. Optimised results can be used directly for experimental work. In this thesis work, we performed a micro-drilling simulation on Inconel 625 superalloy using a WC (YU06) micro-drill bit in Deform 3D v13.0. We observed the feed rate is the dominating factor when compared to the spindle speed.

Keywords: Inconel 625 superalloy, Deform 3D.

TABLE OF CONTENTS

1. INTRODUCTION

We are going to discuss superalloy and types of superalloys, how the formation of superalloy takes place, how alloying elements play a major role in superalloy and what kind of phases are formed, which enhance the mechanical properties and different types of micro-drilling and their applications.

1.1 Superalloys

Superalloys are also called high-temperature alloys. The superalloys show better strength and corrosive resistance even at high temperatures compared to other Fe and Ti-based alloys. Because of these inherent properties of superalloys, demand for such superalloys increased, leading to continuous research and development of superalloys. However, these alloys were not taken into consideration until gas turbine engines were developed. Previously the inlet temperature required for the turbine inlet was 550 °C and the requirements were fulfilled by the stainless steel. Later, the inlet temperature requirement for the flight of Hans Von Ohain's turbine engine Heinkel in Germany and the flight of Whittle's engine in England was beyond 780 °C, the stainless steel cannot withstand that temperature. So, the stainless-steel alloys were heavily modified to withstand high temperatures and that leads to the development of Superalloys [1]. More advancements were made during World War II for military purposes and later the advancements were used for industrial purposes.

These superalloys are used in various complex processes and various operations in various sectors like defence, marine, aerospace, oil and gas applications, etc. Industries need materials with high strength and high corrosive resistance properties, which only the superalloy possesses. Increase in demand for materials for aerospace, defence, and marine applications, the superalloy's global market value goes on increasing. Countries possessing large markets are India, China, South Korea, Japan, and Russia. North America possesses the second largest market primarily the US. European countries make contributions through automobiles [2].

Several countries are heavily investing in defence and aerospace to fulfil the needs of military success and defence strategies, this boosts the productivity of superalloys. Not only in defence and aerospace but also in energy sectors like nuclear power plants by producing steam at high temperatures. These things boost the sales of superalloy.

1.2 Superalloys' effect on alloying elements

Alloy is made to obtain desirable properties, which can be resistance against corrosion, ease of machining, strength, etc. The material properties entirely depend upon her the alloying elements are completely dissolved in the solution or there is a formation of precipitates which leads to different phases, which do not match with the parent material. The alloying elements are generally classified into three groups [3]:

Solid solution hardener:

Chromium, Aluminium, Titanium, Molybdenum, Nickel, and Tungsten all contribute to the strengthening of solid solutions. These solutes also stabilise the FCC structure of the solid solutions of iron and cobalt in the corresponding superalloys and are potent carbide formers, while Cr and Mo encourage the formation of borides as well**.**

Intermetallic hardening phase former:

Atomic radii in the phases generated may be larger than in the parent material. Gamma (γ') Ni_3(Al, Ti), gamma (γ'') Ni_3(Nb, Ta, Ti), and other phases boost the alloy's high-temperature strength and creep deformation resistance. Haynes 242 and 244 alloys were developed as a result of the discovery of another intermetallic phase in nickel alloys with the stoichiometry Ni_2(Cr, Mo, W) [5].

Grain boundary strengthener:

In addition to creating grain boundary precipitates, elements including boron, carbon, zirconium, and hafnium also serve to enhance grain boundaries. The atomic radii of the elements vary greatly from those of the base element. Minor additions result in borides and carbides.

Small amounts of silicon, phosphorus, sulphur, oxygen and nitrogen weaken the alloy by segregating at the grain boundaries.

Connecting with tramp elements, magnesium, manganese, and other elements such as titanium and niobium aid in the removal of certain effects. The elimination of sulphur and nitrogen is aided by the bonding of Mn with S to generate MnS and Ti with N to form TiN.

Al, Mo, Ti, and W help alloys resist environmental deterioration because Cr is transformed to Cr_2O_3 on their exterior surfaces. Its oxidation resistance is improved by Al. The Cr_2O_3 layer is shielded by Mo and W in a variety of corrosive conditions. [1]. Cr is the main solute for hot corrosion resistance, and adding Lanthanum, Yttrium, and Cerium helps to increase high-temperature oxidation and corrosion resistance as well.

1.3 Superalloy formation

Superalloys are made using the double melting method. As we can observe from the Fig. 1.1 describing the superalloy formation through a flow chart, Vacuum Induction Melting is the first step, and then vacuum arc remelting or electro-slag remelting come next. The initial step in the production of cast alloys and wrought alloys is vacuum induction melting. Some oxide particles are still present in the finished product despite the process's success in reducing the amount of oxygen and nitrogen. Additionally, some high vapour pressure particles such as lead and bismuth, are removed. The superalloy's fatigue life is improved by the vacuum induction melting method.

Because the types of impurities present vary, the ingots created by vacuum arc and electro-slag remelting are fundamentally different. Therefore, ingot faults are unique.

In vacuum arc remelting, high vapour pressure particles like lead and bismuth are eliminated to enhance the physical and chemical properties which Vacuum Induction Melting does not eliminate. Magnesium is another high vapour pressure element that is eliminated [5].

In Electro Slag Remelting process helps in the reduction of sulphur content. The high vapour pressure elements like magnesium also get removed in this process but in smaller amounts compared to vacuum arc remelting.

However, some highly alloyed superalloys, such as IN-100, RENE-95, Stellite 31, and others, are made using a powder metallurgy technique. Other superalloys are typically forged or rolled into sheets or other products of various shapes.

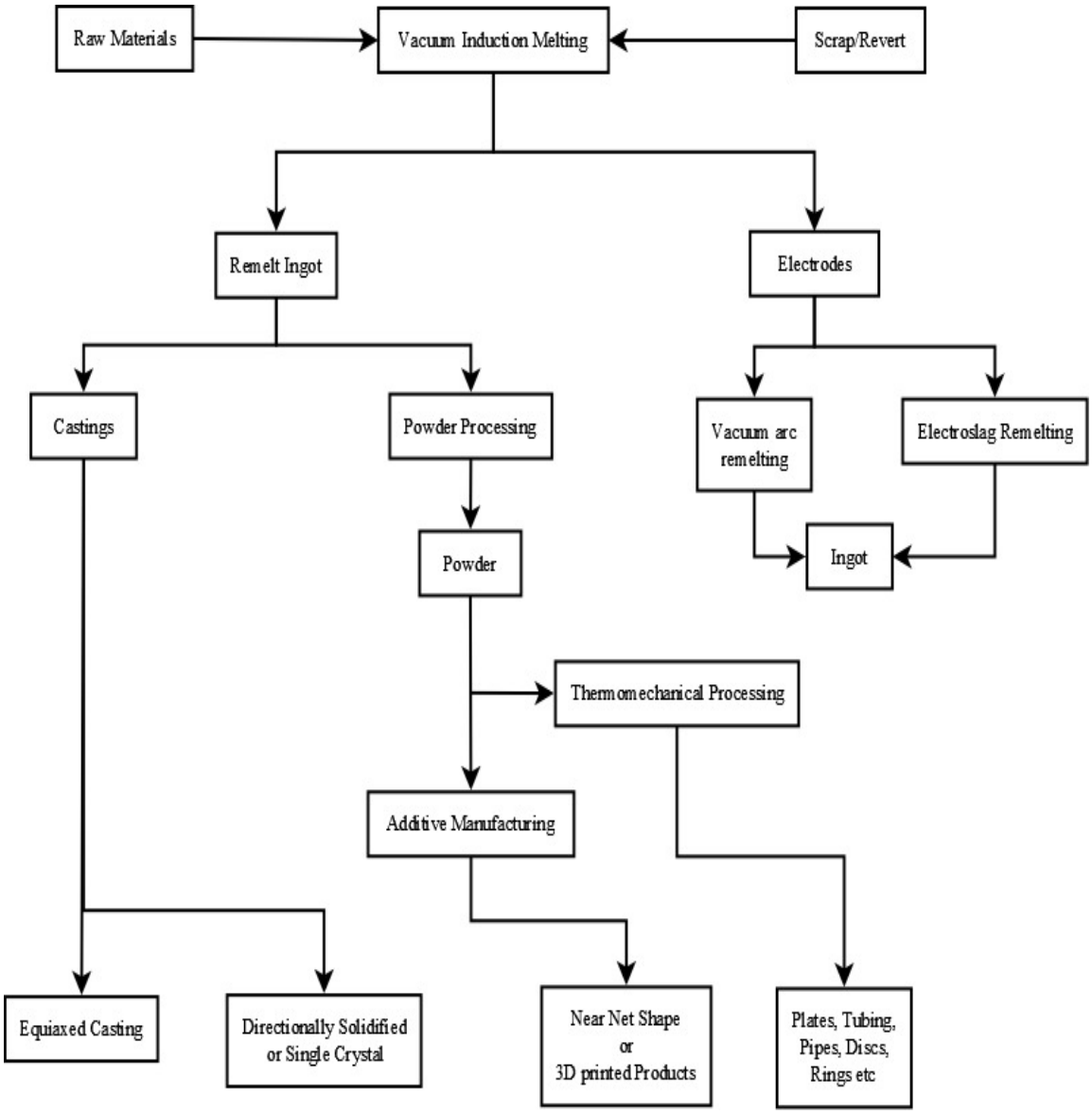

Fig.1.1: Flow chart of Superalloy formation [5]

1.4 Nickel-based superalloy

Nickel-based superalloys are having maximum contribution in superalloys around 80%. These are mostly utilised in hot areas of jet engines. Among the superalloys, these are the most complicated. Nickel is made up of an FCC structure. The proportion of nickel in a nickel-based superalloy will be at least 50%, while the other alloying elements include chromium, which is present in minor amounts, hafnium, zirconium, and combinations of titanium and aluminium up to 8%. There are also some other common elements added, such as niobium, molybdenum, tantalum, tungsten, and rhenium. When exposed to high temperatures and stresses, nickel-based superalloys perform better than cobalt and iron nickel-based superalloys. These Nickel-based superalloys are categorised into two types:

Solid solution strengthening:

The Ni-matrix solid solution strengthens these alloys. Ex: Haste alloy N, Inconel 600, Inconel 690, Inconel 625, and Inconel 617, among others.

Precipitation strengthening:

By precipitating intermetallic compounds, these alloys are strengthened. According to their stoichiometry, these alloys are categorised in two ways.

a) Intermetallic precipitates of $Ni_2(Cr, Mo)$:

ex: Haynes 242, Haynes 244

b) Intermetallic precipitates of Ni_3X:

Precipitates of $Ni_3(Al, Ti)$ (γ' phase):

As the percentage of γ' increases, resistance at elevated temperature increases. Based on the percentage of γ' distribution, there are two types of alloys. The alloy which is having a percentage of about 20-45% of γ' are wrought alloys and a percentage of about 60% are cast alloys. An example of wrought alloys is wasp alloy and an example of cast alloys is Rene 80.

Precipitates of Ni_3Nb (γ'' phase):

The alloy having a γ'' phase possesses good strength at elevated temperatures with better corrosive resistance. This super alloy is highly preferred at elevated temperatures. ex: Inconel 718, custom age 625+.

1.5 Cobalt-based superalloys

The Hexagonal packed structure of pure cobalt is what it looks like at lower temperatures. At higher temperatures, it changes into FCC. The FCC-structured alloying element nickel stabilises the austenitic cobalt structure. Cast cobalt alloy has a composition of 50–60% cobalt, 20–30% chromium, 5–10% tungsten, and 0.1–1% carbon. While 20% of high nickel components and 40% of cobalt are present in wrought cobalt alloys. In cobalt-based superalloys, precipitates don't form [1]. As a result, the alloy is strengthened by carbides and a solid solution. It is a corrosive-resistant substance because of the presence of chromium. With super alloys based on nickel, this alloy's qualities fall short. Examples include Haynes 25 and 188.

1.6 Iron-nickel-based superalloys

Superalloys with an iron-nickel base were developed from austenitic stainless steel that contained 25% nickel. The alloy is strengthened by precipitation hardening with the addition of titanium, niobium, and aluminium as well as solid solution strengthening with the inclusion of the alloying ingredient molybdenum. For instance, Incoloy 903.

1.7 Inconel 625

Due to the mixing of nickel, chromium, and molybdenum used to make Inconel 625, this material has great strength, excellent fabrication, outstanding weldability, and strong resistance to corrosion. The company's market share in nickel-based super alloys keeps growing [6]. We can see the composition of Inconel 625 in the Table 1.1.

This alloy, which is specifically utilised in steam power plants' turbines because it has great strength and good corrosion resistance at high temperatures, can be employed. Niobium and molybdenum were utilised to improve high strength at room temperature.

Table 1.1: Composition of Inconel 625:

ELEMENT	Ni	Cr	Mo	Fe	Nb+Ta	Co	Mn	Al
Wt.%	58-71	21-23	8-10	5	3.2-3.8	1	0.5	0.4

Because of the increased percentage of chromium and molybdenum, which boosts the strength of the solid solution and provides great corrosive resistance to oxidation, we now employ this alloy Inconel 625 at temperatures ranging from cryogenic to 980°C. This alloy has superior fatigue, thermal fatigue strength, resistance to oxidation,

sulfidation, and carburization as well as excellent braze ability and no requirement for post-weld processes due to the presence of niobium. It also has high strength at room temperature and high corrosion resistance.

This material is widely used in a variety of petroleum and chemical industries, heavy water plants, and marine engineering because it has better physical and chemical qualities. This material is utilised in nuclear reactors because it has great resistance to pitting at high pressures and temperatures.

Designers are glad to create designs for high-temperature requirements, such as nuclear reactors and F1 race cars for their exhaust because they have high strength at increased temperatures.

1.8 Applications of Inconel 625

Fuel Refining:

High resistance to oxidation and sulfidation at high temperatures are characteristics of Inconel 625. The distillation tower, nozzles, return bends, overhead condensers, and seamless tubes are only a few applications for this alloy.

Seawater Applications:

Strong tensile strength, high corrosion fatigue strength, and resistance to chloride stress corrosion cracking. The metal alloy is used for components of oceanographic instruments as well as boat propeller blades, submarine propulsion engines, naval boat exhaust ducts, submarine transducers, steam line bellows, and electrical cable connectors.

Aerospace industry:

Having high fatigue, creep, and rupture strength, as well as outstanding weldability. This alloy is used in many specific applications, including rocket thrust chamber tubing, fuel and hydraulic line tubing, heat exchanger tubing, honeycomb structures for housing engine controls, spray bars, turbine shroud rings, combustion system transition liners, turbine seals, and compressor vanes.

Chemical processing:

Being strong and resistant to corrosion at high temperatures. For bubble caps, tubing, reaction containers, distillation columns, heat exchangers, transfer pipework, valves, etc., this alloy is utilised in chemical processing.

Nuclear power plants:

Because of its great strength and resistance to corrosion at high water temperatures, this alloy is used in nuclear power plants for stems, tubing, and springs in the core and control rod components of nuclear water reactors [5].

1.9 Phases of Inconel 625

The single-phase solid solution alloy Inconel 625 contains many alloying components. The precipitation of multi phases caused by an increase in the concentration of various alloying elements including chromium, niobium, and molybdenum is what gives Inconel 625 its great corrosion resistance at high temperatures and good strength.

A mixture of two or more chemical elements that have a common lattice structure is referred to as a solid solution. the phrase is used when mixing occurs at the atomic level. There is a size restriction at the atomic level, which explains why some elements do not form solid solutions while others do. Thermal exposure at intermediates, however, results in hardening and a loss of ductility and toughness. The precipitates that occur as a result of hardening are listed below**.**

Gamma (ɣ'):

This phase is entirely composed of nickel, which has an FCC structure and a structure resembling that of aluminium.

Gamma double prime(ɣ"):

This phase has a structure of ordered body-centred orthorhombic. Consisting alloying elements like Nb, Ti and Al are combined to form a precipitate with Nickel which leads to Ni_3(Nb, Ti, Al).

Delta(δ):

This phase has a structure of ordered body-centred orthorhombic. This precipitate has a combination of Ni_3Nb.

Some phases are in the combination of Cr_2C_6, (Cr, Mo, Ni)$_6$C, (Nb, Ti)C, Mo_6Ni_7, (Cr, Ni)$_2$ (Si, Nb, Mo)Ni_3Mo_2Si having structures with complex cubic, complex cubic, hexagonal, hexagonal respectively [5].

1.10 Micro-drilling

There are two methods, known as conventional and non-conventional processes, for performing micro-drilling operations. In conventional micro-drilling when the workpiece is fixed and the drill bit penetrates the workpiece with translational and rotational motion [20].

Depending on the hole's diameter, micro drilling is defined. The micro-drill bit diameter should fall within the range of 0.05mm and 2.5mm, according to Sphinx, a Swiss manufacturer of micro-drills [7]. The micro-drill bit is defined by Zhuang [8] as having a diameter of less than 3.175mm. Micro-drill bits are those with a diameter of less than 1 millimetre, according to Tibar et al. [9]. According to Kudla [10,11,12], micro-drill bits have a diameter of less than 0.5 mm, and they also indicated that the diameter of a micro-drill can be less than 1 mm [13].

Conventional micro-drilling techniques

Twist type:

When compared to other drill bits, the twist drill type is the most effective since its cutting part has the best shape. The limitations of micro drill bit sizes and the short tool lifespan caused by frequent tool breakage are disadvantages of the twist type [14]. These twist types typically break down before they wear out and cannot offer the mechanical strength needed to sustain the cutting forces. The following SEM images are shown in Fig. 1.2, the tool material is tungsten carbide with 0.01mm diameter.

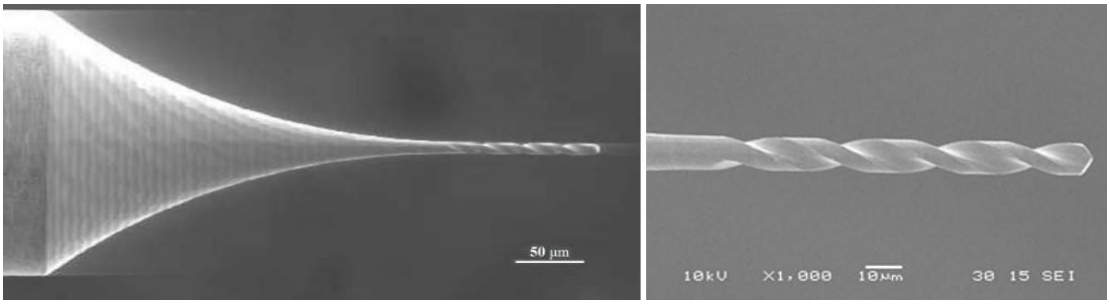

Fig. 1.2: Twist drill type [15] d=0.01mm WC

Spade type:

It is the tiniest of all, having a diameter of less than 10 mm. In a twist type, this kind of diameter is not feasible. An SEM image shown in Fig. 1.3 tells that because there are no helical flutes in this drill bit, its cutting capacity is less than that of a twist type, and

chip removal is more difficult. Poor surface roughness is the result of excessive feed rates.

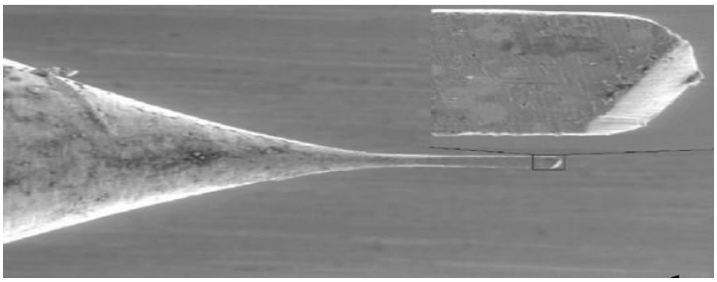

Fig. 1.3: Cutting part of spade drill type d=0.0125mm [15,21]

D-shaped type:

These micro-drill bits are less than 0.05 mm in diameter. From Fig. 1.4 we can see that these micro-drill bits are made in a straightforward manner. However, because fewer chips are being removed, cutting performance is poor. These drill bits are not as common as twist drill bits.

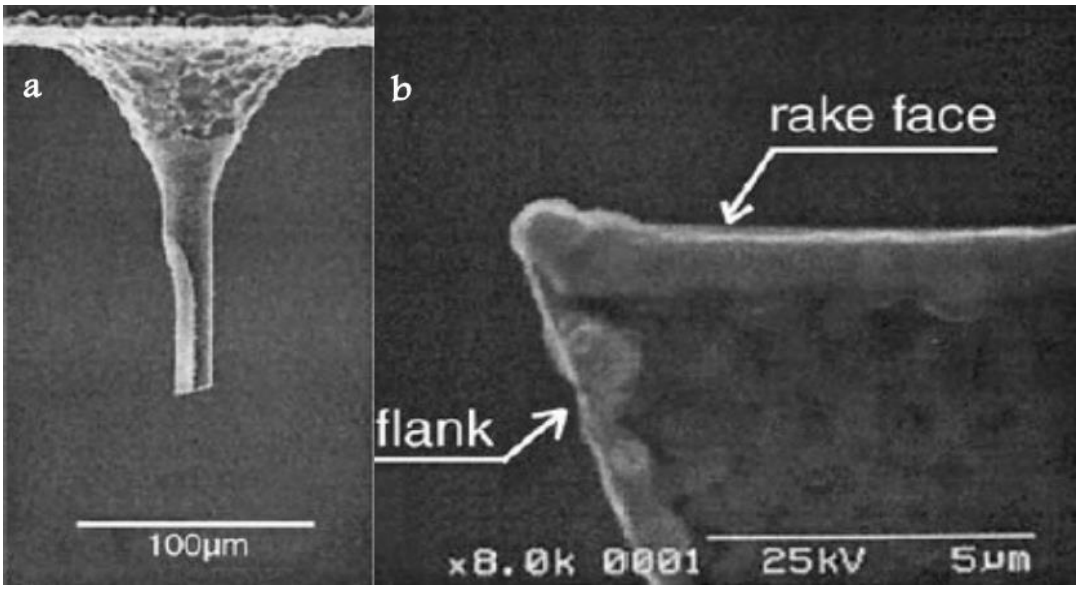

Fig. 1.4: SEM images of D-shaped micro-drill a) overview b) close up view showing rake face [22,16].

Single flute type:

Fluted micro-drills can be used to decrease drill bit breakage. Because fewer chips are removed when used, less heat is generated between the micro-drill bit's contact region and the work piece. Drill breakage is decreased as a result. The cutting speed of a single flute micro-drill bit is half that of a twist type micro-drill even with the same spindle speed and feed rate [17,18].

Compound type:

This particular type of micro-drill bit has abrasive particles. There is a burr formation at the beginning and end of the work piece following micro drilling using standard micro-drill bits. Therefore, compound micro-drill bit is employed to reduce burr development [19]. As we can see abrasive particles on the other side of micro-drill bit in the Fig. 1.5.

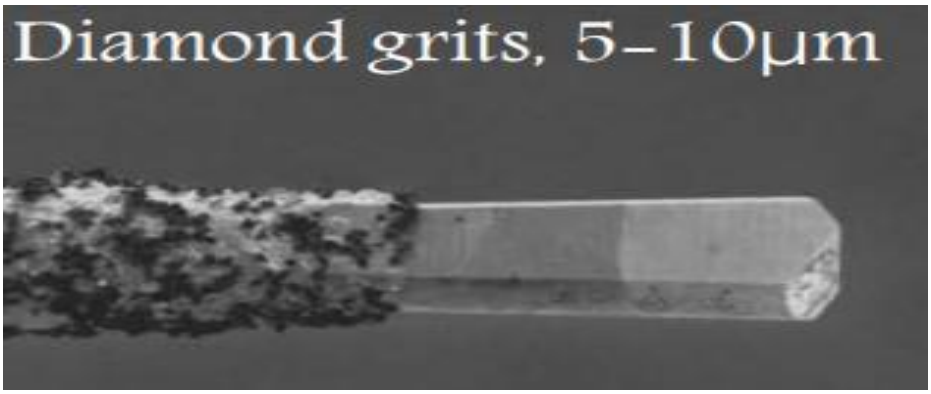

Fig. 1.5: compound micro-drill with abrasives over it [19].

Non-conventional Micro-drilling techniques:

Laser micro-drilling:

It is the most common operation, and the outcomes include poor dimensional precision, the development of a recast layer, the presence of residual stresses that result in microscopic cracks in the hole, and high production costs. These flaws are influenced by the laser's power source, focal length, irradiation time, pulse width, air pressure, and the state of the surrounding gas**.**

EDM micro-drilling:

No matter the geometry or level of hardness of the work piece, if it is electrically conductive, this method can be applied. However, there are little cracks and a poor surface finish in the work piece. The system parameters are the only factors affecting the flaws.

Electro chemical micro-drilling:

This technique is employed for high production and material removal rates. In comparison to conventional one, the dimensional precision is poor.

Electron beam micro-drilling:

The creation of tiny holes using an electron beam is a new technology. Bulk micro-holing for complicated forms is mostly what it's utilised for. Poor overall quality, high investment and high-power usage.

Ultrasonic Vibration in conventional micro-drilling:

Ultrasonic vibration is employed in micro-drilling, which is primarily used to create superior quality micro holes. However, complex shapes cannot be used, and the work material must have a certain hardness rating. The pace of production is relatively slow.

2. LITERATURE REVIEW

In machining operations like turning and milling, the chip removal process is much easier compared to drilling. In drilling operation, as the tool moves along the thickness of the work piece, there is lot of heat generation, use of coolant is also not effective as there is very small clearance between the tool and the workpiece. Accuracy of the drilled hole is also not good. Chances of tool breakage and tool wear are more. So, in order to increase the hole quality and to decrease tool wear and tool breakage, many researchers have proposed various improvements in techniques and methods regarding tool material, tool geometry, parameters used in performing drilling operation, use of lubrication and tool coatings.

According to Armarego [24] in his work, practical aspects of twist drills, a drill geometry having two flutes is required for maximal material removal. We must take into account the three phases of drilling operations: the start and centring phase, the complete drilling phase, and the break through phase. The chisel edge of the cutting tool must make contact with the work piece during the starting and centring phases in order for the hole to be accurate. According to C.J. Oxford [25], if the chisel edge's centring is weak, this causes tool vibration and tool breakage. In full drilling phase there are frictional effects between the margins of drill bit, chip against the workpiece and we can also observe changes in mechanical and thermal behaviour. In break through phase, we can observe the penetration of drill tip through the workpiece and elastic deformation of the workpiece which leads to the formation of burrs at exit.
Amarego [24] adds that the effectiveness of the drilling process depends on a number of variables, including thrust, torque, tool life, component accuracy, and the workpiece and tool's surface quality. And according to Galloway et. al [26,27], whose work is related to improving drilling techniques, performance is also influenced by the properties of the materials used in the work piece and the tool, tool geometry, cutting conditions, cooling lubricants, and the machine tools employed. They also stated that small variations from the aforementioned parameters result in ineffective operation.

Drill point geometry in drilling operation plays a major role of principal parameters, the entire efficiency of this operation depends on the drill point geometry because this is

the part where material removal is involved. The drill point geometry value varies differently for different materials stated by Cheong et. al [28]. The drill point geometry, according to M.C. Shaw and Amarego [29,24], contains the nominal diameter, the web thickness, and the helix angle at the perimeter. According to G. Spur and Masuha [30], the chip can be transported and evacuated more easily with the help of the point angle, the lip clearance angle at the perimeter, and the helical profile flute. According to Shaw [29], the point angle, web thickness, and helix angle all have a significant impact on how well drilling operations go because they have an immediate impact on the normal and effective rake angles of the twist drill point.

2.1 Significance of helix angle

In their experiment, Agapiou et. al [31] found that the helix angle impacts the effective rake angle, which results in a modest decrease in tool tip temperature. When the variation in helix angle is between 15° and 40°, as Shaw and Oxford [32] discovered, torque and thrust forces on the drill similarly decrease. They are lowered to between 0.6% and 0.4% per degree increase in helix angle. A high helix angle value produces effective chip removal, whereas a low helix angle produces ineffective chip removal and a high cutting edge. Spur and Mausha [30] also stated that a high degree of stiffness should be included in the tool to prevent drill breakage. According to Kronenberg [33], having a high helix is inefficient during drilling operations due to an increase in thrust force. Using the finite element simulation technique, Muthukrishna and Sujatha [34] investigated the lowest radial deflection and concluded that the ideal helix angle should be about 40°. In his experiments, W.C. Chen [35] found that the axial displacement rises as the helix angle exceeds 30°. Here, we can observe that the ideal helix angle is changing. Varied materials may require a different helix angle.

2.2 Significance of Web Thickness

Shaw [29] advises that for hard materials, the web thickness should be greater because it is crucial in strengthening the cutting edge close to the drill point. According to W.C. Chen [35], an increase in web thickness leads to an increase in chisel edge length, which increases material removal. According to Galloway [26], however, when web thickness grows, there is a reduction in the flute regions, which reduces chip evacuation and increases thrust force. The overall thrust force and torque are enhanced by 60% and

22% as a result of an increase in chisel edge length, according to Shaw and Oxford [32] and J. Audy [36] analyses of the effects of increasing web thickness on the torque and thrust forces.

The second moment of inertia and cross-sectional area affect torsional stiffness. According to Thornley et. al [37], torsional rigidity plays a crucial part in the ability to tolerate large axial stresses during drilling operations. However, according to Spur and Mausha [30], increasing web thickness causes a decrease in torsional rigidity. According to Narashmha et. al [38], an increase in web thickness causes a reduction in the torque-thrust interaction and lowers stiffness. The ideal stiffness value should depend on the material being used, according to Spur and Mausha [30]. For strong materials, stiffness should be taken into account in order to withstand high thrust forces and extend tool life.

2.3 Significance of Point Angle

According to C.J. Oxford and Galloway [26,25,27], low point angles are used for low strength materials and high point angles are chosen for high strength materials. For hard materials, the point angle should be greater because an increase in point angle causes a rise in effective rake angles, which has a greater impact at the chisel edge than at the periphery. Therefore, tougher material should be cut with strong cutting force using tools with high point angles. Additionally, low point angles for low strength materials cause the effective rake angle to grow towards the periphery rather than at the chisel edge in order to accommodate low cutting forces. According to Shaw [29], drill bit failure occurs at the perimeter for ductile materials and in the centre for hard materials. M. Field et. al [39] said more about point angle for nickel-based super alloys.

According to M.C. Shaw and J. Audy, when the point angle increases, the torque decreases and the thrust forces increase [32,36]. Longer cutting edges and greater material penetration would result from having large point angles. According to Agapiou et. al [31], shorter cutting-edge length raises the temperature at the cutting tool's tip. Increased point angle values result in flattening of the workpiece and difficulty centring, which causes drilling to be less precise.

2.4 Micro machining

According to J. Chae and X. Liu et. al [41,42] observation's, the use of highly accurate tiny components has grown in the automotive, aerospace, biomedical, and electronics industries. We cannot easily extrapolate macro-drilling rules to micro-drilling due of the numerous challenges with micro machining, including chip formation mechanisms, minimum chip thickness, vibrations, excessive stresses, and difficulty in analysing these components. According to Kudla et. al [11], the heat dissipation in the micro-drilling process differs from the macro-drilling process because in the macro-drilling operation, chips are continuously formed and between 70% and 80% of the heat is dissipated by the chips. According to D.A. Lucca et. al and J.D. Kim et. al [43,44], shearing in the shear zone and rake face friction were not regarded as absorbed energies in macro-drilling as the depth of cut decreased. The elastic property of the work piece is replaced by the tool flank face rubbing action against the work piece in the case of small tools.
Inamura et. al [45]'s analysis of the energy dissipation during the micro-cutting of copper revealed that around 43% of the total energy was lost by plastic deformation into the deformation zone.

2.5 Micro-drilling operation

Cheong et. al [28] describe micro-drilling as having an aspect ratio greater than 10 and a tool diameter less than 0.5 mm. Based on a tool's cross-sectional profile and web thickness, Kudla [46] defines micro-drilling.
The conventional micro-drilling procedure yields holes with good cylindricity, a smooth surface, and extremely acceptable results. However, creating holes with accuracy is a challenging process; occasionally, the drill tip breaks inside the work piece, causing money to be wasted, according to Kudla [47]. Additionally, there are mechanical issues such as decreased mechanical strength, high temperature heat zones, decreased speeds and feed rates, increased thrust and torque, and burr development. According to M Imran et. al's research [71] utilising a nickel-based work piece and a tool with a WC of 0.5mm, sharpness is crucial. In micro-drilling, the usual macro-drilling parameters are useless.

For large diameters, the chisel edge length to the diameter is quite low, hence the radial forces are insignificant. However, for micro-drills, the ratio of the chisel edge length to

diameter is very high, and as stated by Kaminski et. al [48], we cannot ignore radial forces. Therefore, the work piece should be flat with a good surface finish, and we need to be careful about centring because, as stated by Y. Gong [49], small radial forces can cause drill skidding during the initial penetration stage. According to kaminski et. al [48], employing smaller flute drills with a shorter length is preferable than utilising larger flute drills for preventing skidding and deviation. Because of this, pilot hole drills have short flute lengths to reduce skidding.

2.6 Stiffness's function in micro-drill bits

Drill bit damage occurs during micro-drilling operations. Drill performance may be significantly impacted by stiffness, micro-drill bit strength in bending, torsion, and complicated loads, among other factors that contribute to drill breakage. According to Oxford [50], if a drill bit's length is greater than its diameter, a reduction in stiffness will result, which will cause the drill bit to break before it wears out. Torsional stiffness is directly proportional to the fourth power of drill bit diameter and inversely proportional to its length. According to Y.Gong [49], the bending stiffness is similarly poor for micro-drill bits with long lengths, which causes them to first buckle and then break.

2.7 Effect of torque and thrust

Torque and thrust play a significant role in micro-drill bit fracture as well. According to Z. Yang et. al [51], the thrust and torque forces were observed to be stronger at early penetration and the initial cutting forces are higher. The torque and thrust forces increase as the drill depth increases, however according to Iwata [52], at the moment of drill breaking, the torque is higher and the thrust is lower. When a chip from the cutting process comes into contact with the tool, friction is created, the temperature rises, and the hardness of the tool is subsequently decreased. According to Aronson [53], it is especially challenging for workpiece materials with low thermal conductivity. In a micro-drilling operation, the retraction process aids in chip removal and allows lubricant to flow into the work piece, cooling the drill bit. Rahamathullah and MS Shunmugam [70] employed a variety of techniques, including direct drilling of blind holes, peck drilling of blind holes, and peck drilling through holes. Their findings indicate that peck drilling produces lower thrust forces and increases tool life.

2.8 Effect of speeds and feeds in micro-drilling

In the machining process, cutting conditions are crucial. According to Lee et. al [54], the dominant factor in the micro-drilling process that affects the chip thickness and cutting forces is the feed. According to Iwata [52], cutting pressures are not the sole factor influencing the quality of the hole. Tool breakage occurs during the micro drilling process due to high feed rates. According to the results of the Kudla [55] experiment, the micro drilling operation is significantly influenced by the length of the stroke, feed rate, accelerations, deacceleration, and retraction process. High speeds cause an increase in temperature in poor thermally conductive materials while also reducing torque and thrust forces due to thermal softening. According to a simulation of micro drilling by Hongyan et. al [68], feed rate is more important than high speeds, where thrust and temperature are more important. According to M. Imran et. al [71], when the feed is smaller than 0.005mm/rev, the tool life is lowered in micro-drilling.

2.9 Tool wear's impact

The choice of cutting tool is crucial for processing nickel-based super alloys. High speed steel (HSS), tungsten carbide (WC), ceramic, and cubic boron nitride are the cutting materials employed. According to Sims et. al [56], these materials have high strength, strong wear resistance and toughness, high hot hardness, good thermal shock capabilities, and stability at high temperatures. The essential factor is that it must keep hardness at high temperatures. Ezugwu [57] claimed that hardness decreases at high temperatures. However, Narutaki et. al's studies [58] show that HSS cutting tools do not work well with nickel-based super alloys since they have a low softening temperature of roughly 550°C. Similar findings were made with the use of ceramic tools, which were shown to be unsuccessful due to their low durability. According to Devillez et. al's experimental findings [59], cemented carbide tools of WC-Co grades were employed for improved machining and outperformed other materials by having high fracture toughness, comprehensive strength, and abrasion resistance. When steel and nickel-based superalloys were machined under identical cutting conditions, the nickel-based superalloys were subjected to higher temperatures and stresses than steels, stated by Wright and Chow [60] and mentions that there are significant rates of tool wear.

2.10 The impact of Cooling

According to Klocke and Eisenblatter [61], adding coolants has a significant impact on chip removal, heat dissipation from the cutting zone, and lubrication between the tool and the work piece. According to Z. Yang et. al [52], the main justification for utilising coolants is typically when drilling small holes because higher friction could encourage rising cutting temperatures and shorten tool life. According to Kudla and X. Yang et. al [46,62], the torque and thrust forces were also decreased with the application of cooling lubricants. Due to the high temperatures produced during micro drilling, the workpiece's subsurface is destroyed. According to Chen [63], the use of coolant lubrication results in a decrease in subsurface damage and an improvement in tool life. According to Jung Soo Nam et al. [69], compressed air lubrication and nanofluid lubrication both reduce thrust forces and torque. They also claimed that nanodiamond particles make nanofluid lubrication more effective, but that increasing the amount of these particles also increases thrust forces.

2.11 Tool coatings' impact

We employ coatings to prolong the life of the tool. According to Devillez et. al and Ezugwu et. al [59,64], coated carbide tools have been utilised to increase the machinability of nickel-based superalloys by reducing tool wear. According to Karmer [65], an imbalance in the young's modulus of the coating and the tool causes an increase in load and stress levels. According to research by Donald et. al [66], coatings offer great wear resistance as temperature rises and also offer chemical stability. Additionally, a superior surface quality is attained, compressive stresses are reduced, and thermal conductivity and oxidation resistance are provided. In particular during drilling, the coating should be able to provide strong thermal conductivity and be able to drain energy from the cutting zone. In their experiment, Philip A. Primeaux et. al [72] used coated and uncoated carbide drill bits to micro-drill hard Ni alloys. They reported that while TiAlN coating on carbides increased tool life by about 50%, cutting performance decreased, built-up edges were noticed, and material adhesion occurred as a result of adiabatic heating. They claim that lubrication is essential. The experiment by A. Thakur et. al [73] looked at the impact of cutting speed and CVD multilayer coating on Inconel 825 during drilling operations. They compared CVD multilayer ($TiN/TiCN/Al_2O_3/ZrCN$) cemented carbides that were uncoated and coated. They

discovered that using CVD coating, which provides a surface with less hardness, reduces the production of white layer. Additionally, A. Thakur et. al [74] reported that when coating a tool with CVD during a turning operation, a higher surface quality and a thinner White layer were seen.

2.12 Inconel 625's dynamic behaviour

According to Hokka et. al [67], the simulation findings were insufficient when compared to the experimental outcomes obtained using the Johnson Cook Model, which exhibit safer outcomes at greater strain rates. They changed the J C Model in consideration of the experimental outcomes.

3. SIMULATION DETAILS

3.1 Simulation Work

For simulation work, we used DEFORM 3D v13.0 software. It consists of:

- **Pre-Processor**
- **Simulation**
- **Post-Processor**

Pre-Processor

Material selection, geometry, object-positioning, meshing requirements, boundary conditions, and simulation parameters are defined for work piece and tool in the Pre-Processor**.**

General:

The object is often described by its initial temperature and one of its properties (e.g., hard, plastic, elastic, or elasto-plastic). The library's own material parameters are used for the work piece and micro-drill bit, but we can also import data by making a specific file.

Here, the workpiece is assumed to be plastic with an initial temperature of 20°C, and the micro drill bit is assumed to be rigid with an initial temperature of the same value as the workpiece with convection coefficient (0.02 N/s/mm/°C) around it.

Geometry:

Deform 3D software allows us to instantly construct objects for simple geometries; however, complex geometries must be created in Catia or Solid works. Files having .STL extension can be imported into Deform 3D.

The work piece component in this instance has diameter of 0.6 mm and thickness of 0.1 mm as shown in Fig. 3.1, making it simple to manufacture in any 3D software. In contrast, because the micro-drill bit has complex geometry, it was designed in Catia (shown in Fig. 3.2) by considering specific geometric parameters which are mentioned in the Table 3.1. The entire Catia model is exported into Deform 3D software by converting into an STL file.

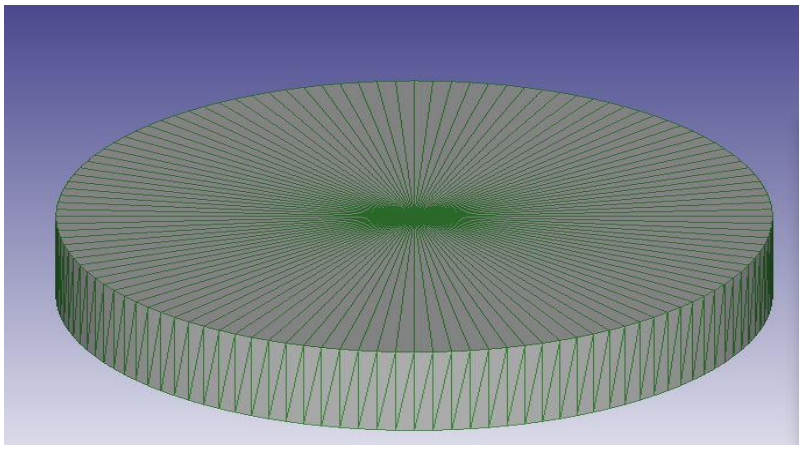

Fig. 3.1: Work piece of diameter = 0.6mm and thickness = 0.1mm built in Deform 3D

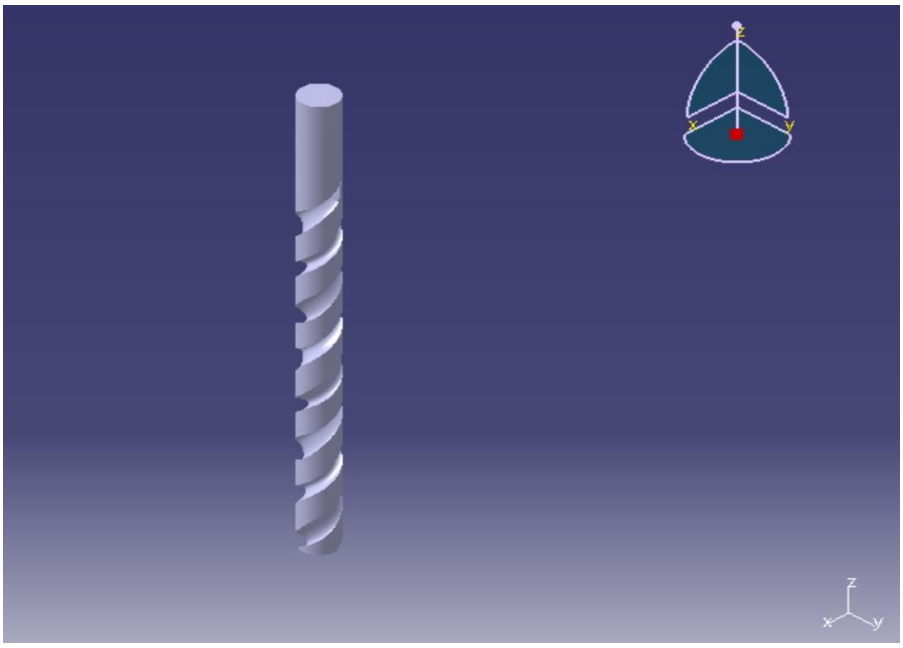

Fig. 3.2: Micro-drill bit Catia model

Table 3.1: Micro drill bit geometry specifications:

Length	4mm
Flute length	3.2mm
diameter	0.3mm
Helix angle	40°
Point angle	130°
Web thickness	0.14mm
Flute and Land ratio	1:2

Material selection:

Inconel 625 was the work piece material in the simulation of micro-drilling, while tungsten carbide is used for the drill bit (YU06). Mechanical properties for both materials are shown in Table 3.2.

Table 3.2: The properties of the materials are:

Mechanical properties	**Inconel 625**	**Tungsten carbide (YU06)**
Young's modulus (GPa)	207	640
Density (kg/m^3)	8440	14700
Poisson's ratio	0.308	0.21
Melting point temperature (°c)	1350	2870
Thermal conductivity at room temperature (W/m k)	9.8	110

Flow stress model for Inconel 625:

The Johnson-Cook model's simulation findings for Inconel 625 were unacceptable because they overestimate the material's strength under high strain rates.

$$\boldsymbol{\sigma} \quad = \quad (\boldsymbol{A} + \boldsymbol{B\varepsilon^n})(\mathbf{1} + \boldsymbol{C}\ \mathbf{ln}\frac{\dot{\varepsilon}}{\dot{\varepsilon}_{ref}})(\mathbf{1} - [\frac{\boldsymbol{T-T_{ref}}}{\boldsymbol{T_m-T_{ref}}}]^{\boldsymbol{m}})$$

$(A + B\varepsilon^n)$ = f(strain), $(1 + C\ \ln\frac{\dot{\varepsilon}}{\dot{\varepsilon}_{ref}})$ = f(strain rate), $(1 - [\frac{T-T_{ref}}{T_m-T_{ref}}]^m)$= f(temp)

σ = Flow stress, A = Yield strength, B = Hardening modulus, Ɛ= strain, X= strain rate, $\dot{\varepsilon}_{ref}$= Reference strain rate, T= temperature, T_{ref}= reference temperature (20°C), C= strain rate sensitivity, T_m= melting point temperature of Inconel 625, n= Strain-hardening exponent, m= thermal softening exponent.

The following Table 3.3 shows certain parameters of the Johnson Cook model along with the corresponding values.

Table 3.3: Johnson cook model parameter values for Inconel 625:

Parameter	**A [MPa]**	**B [MPa]**	**n**	**C**	**m**	$\dot{\varepsilon}_{ref}$ $[s^{-1}]$	T_{ref}	T_m	C_p **[J/Kg]**	ρ $[kg/m^3]$
Values	558.8	2201.3	0.8	0.00021	1.14	1670	20	1350	480	8440

So, we used the modified Johnson-cook model for better simulation results. The modified Johnson cook model is given below

$$(A + B\varepsilon^{n})(\tanh(\frac{1}{\varepsilon^{k}}))(1 + C \ln\frac{\dot{\varepsilon}}{\dot{\varepsilon}_{ref}})(1 - [\frac{T - T_{ref}}{T_m - T_{ref}}]^{m})$$

(Strain softening exponent) K =3 [67]

Meshing:

To obtain the results at every point on the workpiece and tool we use finite elements called mesh elements. The smaller the size of mesh elements, the greater the accuracy of results. However, decreasing the size of mesh elements increases the simulation time. Here, Fig. 3.3 shows mesh diagrams of the workpiece and tool, the element shape is tetrahedral and the initial element size is 0.006mm and 0.02mm for the workpiece and tool respectively are considered respectively by choosing absolute mesh mode with size ratio 4.

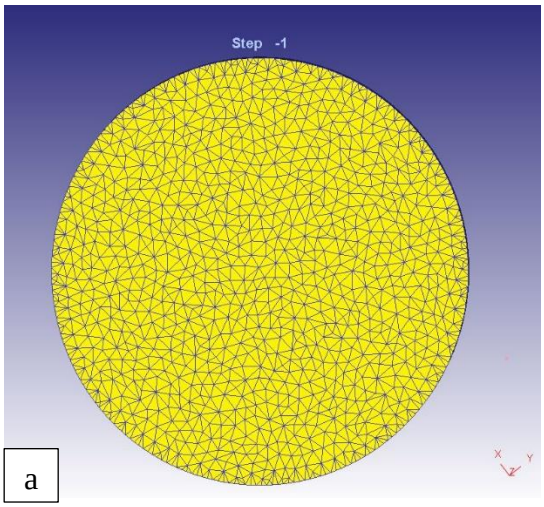

a

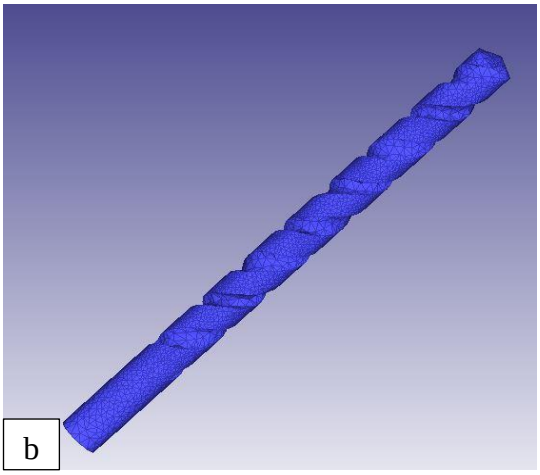

Fig. 3.3: meshing diagrams a) workpiece and b) micro drill bit

To decrease the running time of the simulation we used adaptive meshing. Fig. 3.4 and Fig. 3.5 represent adaptive meshing settings in the meshing window. In the adaptive meshing process, a specified region is selected where the workpiece and tool are in contact where the element size is very small while in the other regions, the element size is relatively larger. The modified size of the mesh element for the work piece is 0.003mm. The adaptive meshed workpiece can be observed in Fig. 3.6.

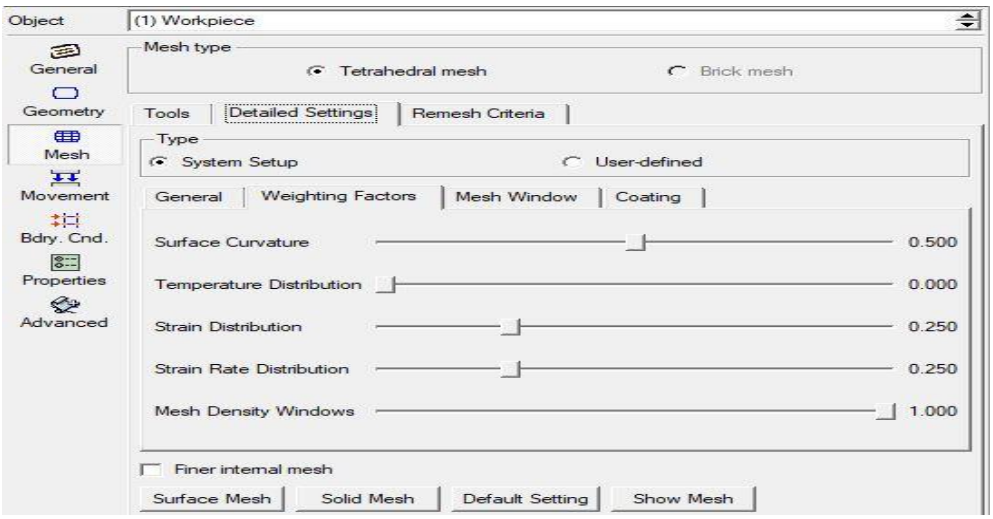

Fig. 3.4: Adaptive meshing details

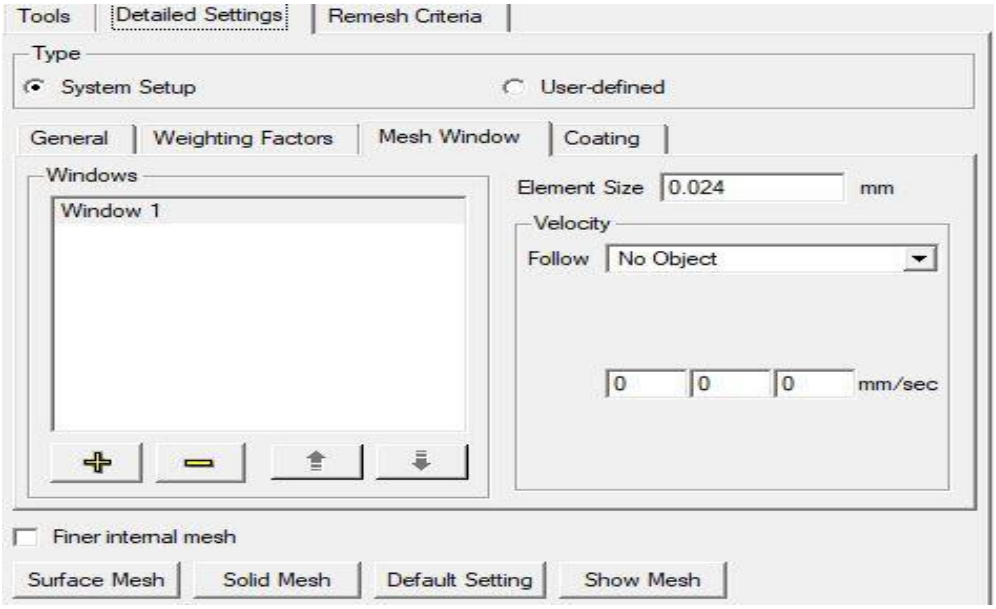

Fig. 3.5: Mesh window for adaptive meshing

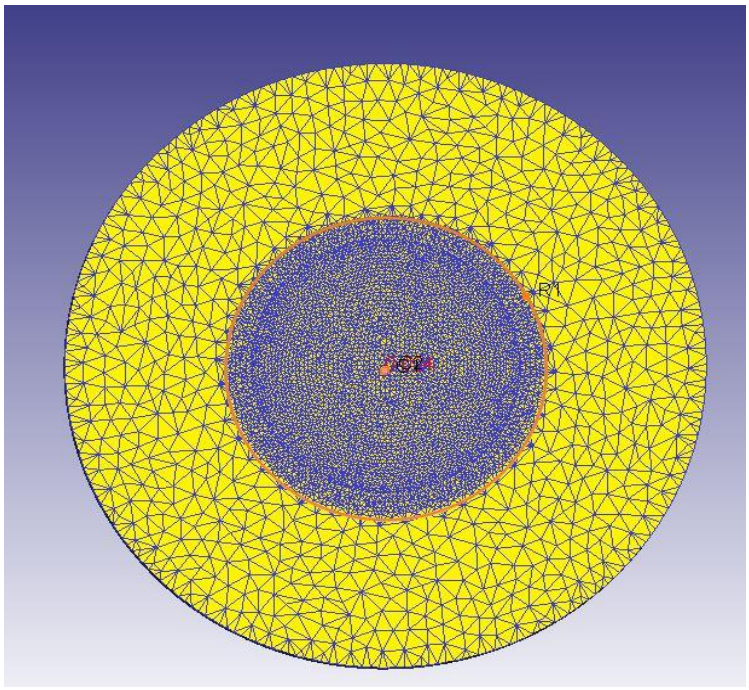

Fig. 3.6: Workpiece after adaptive meshing

Movement:

In movement, we need to define the translational and rotational motion of the workpiece and the tool. In a micro-drilling process where the workpiece is fixed and the tool is moving, we only need to define the translation motion of the tool along (-ve) z direction and rotational motion along z direction (anti-clockwise). The tool rpm values chosen are 50krpm, 80krpm, and 140krpm and feed rate values are 3m/min and 4.8mm/min.

Fig. 3.7 and Fig. 3.8 represent the window for the movement settings along translational and rotational respectively.

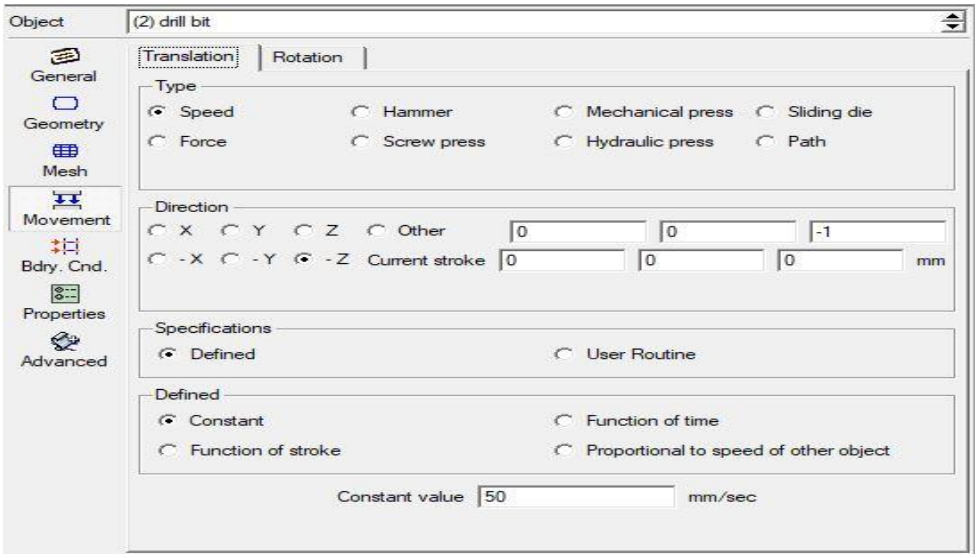

Fig. 3.7: Window for translation motion settings for the tool

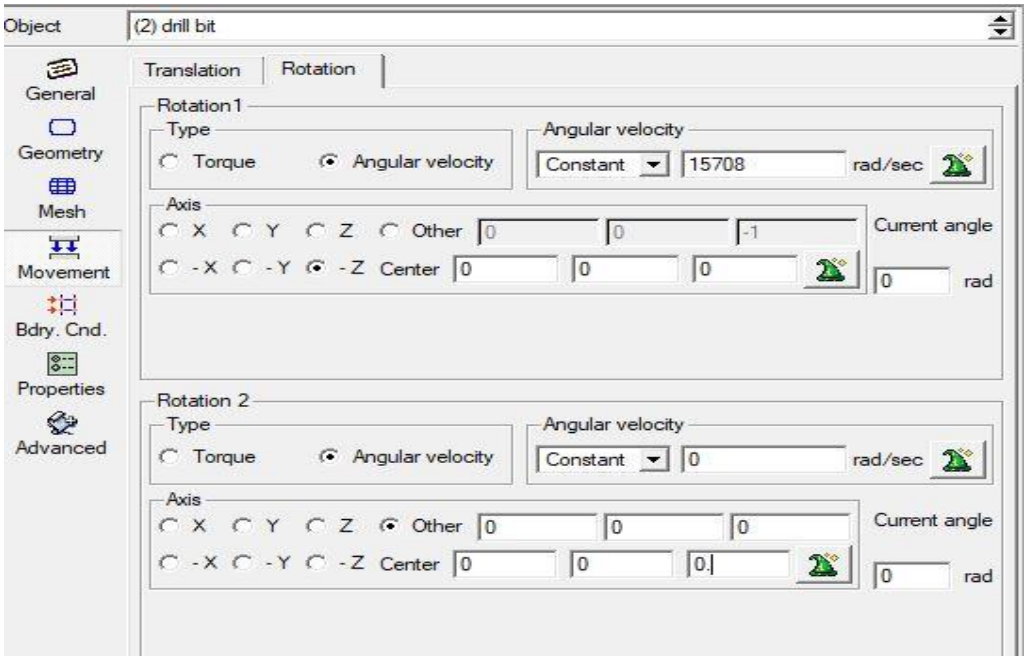

Fig. 3.8: Window for rotational motion settings for tool

Boundary conditions:

We need to apply boundary conditions according to the machining process. For the micro-drilling operation, we need to fix the outer faces of the workpiece. Fig. 3.9 and Fig. 3.10 show the velocity deformation boundary condition along the Z direction (bottom side) and (X, Y) directions (lateral surface) respectively for the workpiece. We

also need to define the heat exchange boundary conditions between the surroundings and for both the workpiece and the tool.

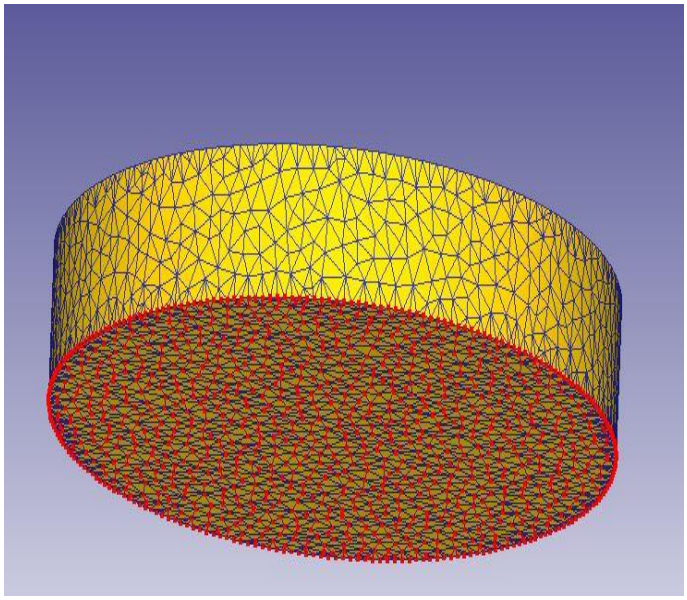

Fig. 3.9: fixing along Z direction for velocity deformation

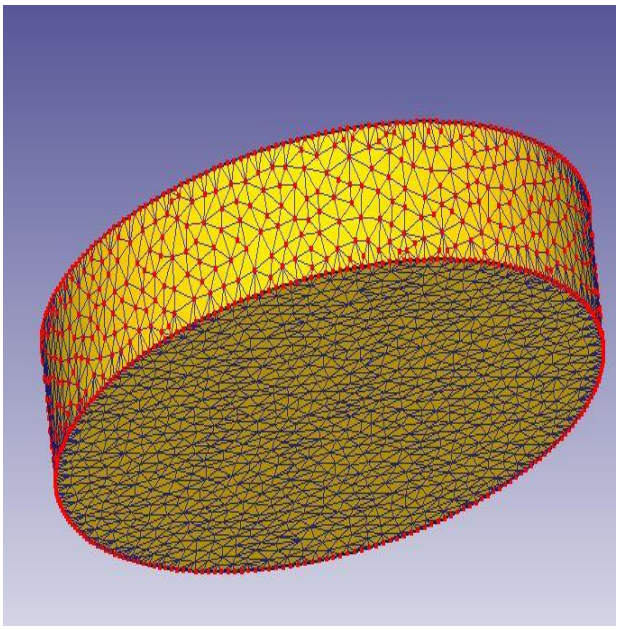

Fig. 3.10: fixing along X, Y direction for velocity deformation

Tool wear calculation:

For tool wear calculation we need to define the hardness property of the tool in terms of HRC (Rockwell hardness with grade C).

Model for tool wear calculation:

Equation $w = \int apVe^{-b/T}\, dt$

P = interface pressure;

V = sliding velocity;

T = interface temperature (°C);

dt = time increment;

a = 0.000000000758, b = 5302 for tungsten carbide [75].

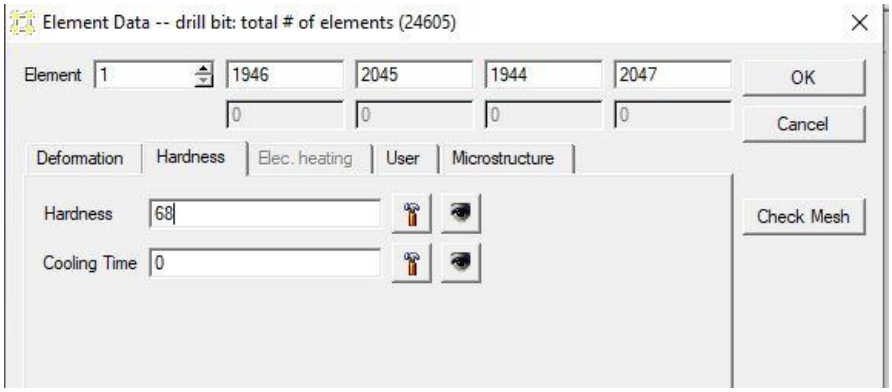

Fig. 3.11: Window for Hardness

Fig. 3.11 shows the window for entering the hardness value for tool wear calculation and corresponding to the hardness value we get tool wear results. The hardness value for tungsten carbide (YU06) is 68 HRC.

Table 3.4: Heat transfer parameter settings:

Environment:	
Temperature	20 °C
Convection Coefficient	0.02 N/s/mm/°c
Tool – workpiece interface:	
Shear friction factor	0.5
Heat Transfer Coefficient	45 N/s/mm/°c

Table 3.4 shows the heat transfer parameter values. Simulation represents actual work which we do in industries involving surrounding temperature, heat transfer coefficient,

and convection. To accurately represent the surrounding environment in simulation, we need to use real values of heat transfer parameters.

Table 3.5: Simulation control settings:

No. of simulation steps	10,000
Step increment to save	10
Time increment value	1.0 e-6s
Iteration method	Newton-Raphson
Solver	Sparse

Table 3.5 shows the simulation parameters, no. of simulation steps indicates how many steps are required to complete the simulation work. If no. of steps is in the hundreds, we cannot observe any simulation work. Simulation work done is saved after every 10 steps, this value can be changed in the "Step increment to save" section. We can observe the movement of the micro-drill bit every 10 steps. The iteration method and solver influence the calculations of stress, strain, temperature, etc values.

After giving inputs to the pre-processor, we saved the details and ran the simulation. After completion of the **simulation** procedure, we can see the entire results in the **post-processor.**

4. RESULTS AND DISCUSSION

Before discussing simulation results, we need to make sure that Deform 3D simulation results are valid. We took the Hongyanshi et. al [68] simulation results as a reference, which deals with Online temperature measurement of micro-drilling using simulation, where Al 6061 with diameter = 0.6mm and thickness = 0.1mm is used as a workpiece and tungsten carbide as micro-drill bit tool of diameter = 0.3mm, helix angle = 40°, point angle = 130° and web thickness = 0.14 mm. The spindle speed = 150krpm, the feed rate = 80 mm/sec and the workpiece is stationary.

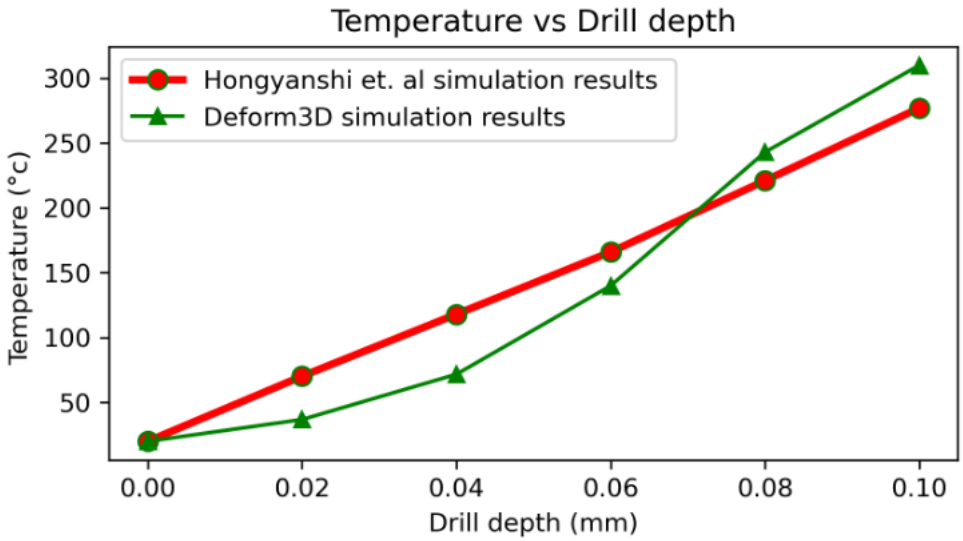

Fig. 4.1: Comparison between Hongyanshi et. al [68] simulation results and Deform 3D simulation results

Fig. 4.1 shows the temperature results obtained from Deform3D software are lower in comparison to Hongyanshi et. al simulation results up to the drill depth 0.06mm and after 0.065mm drill depth Deform3D temperature results are higher than the Hongyanshi et. al temperature results. Here we observe that there are small positive and negative deviations in simulation results which are acceptable.

For all FCC materials Johnson Cook model is used for Finite element simulation. The Johnson cook model for Inconel 625 is as follows:

$$(\boldsymbol{A}+\boldsymbol{B}\boldsymbol{\varepsilon}^{\boldsymbol{n}})(\mathbf{1}+\boldsymbol{C}\ \ln\frac{\dot{\varepsilon}}{\dot{\varepsilon}_{ref}})(\mathbf{1}-[\frac{\boldsymbol{T}-\boldsymbol{T}_{ref}}{\boldsymbol{T}_{m}-\boldsymbol{T}_{ref}}]^{\boldsymbol{m}}) \quad [67]$$

Table: Johnson cook model parameter values for Inconel 625: [67]

Parameter	A [MPa]	B [MPa]	n	C	m	$\dot{\varepsilon}_{ref}$ [s^{-1}]	T_{ref}	T_m	C_p [J/Kg]	ρ [kg/m^3]
Values	558.8	2201.3	0.80	0.00021	1.14	1670	20	1350	480	8440

The Finite element simulation results for Inconel 625 under orthogonal cutting operation using the Johnson cook model do not match with the experimental results. The researchers modified the Johnson-Cook model according to experimental results. The modified Johnson-Cook model is given below.

$$(A + B\varepsilon^{n})(\tanh(\frac{1}{\varepsilon^{k}}))(1 + C \ln\frac{\dot{\varepsilon}}{\dot{\varepsilon}_{ref}})(1 - [\frac{T-T_{ref}}{T_m-T_{ref}}]^{m}) \quad \textbf{[67]}$$

k =3

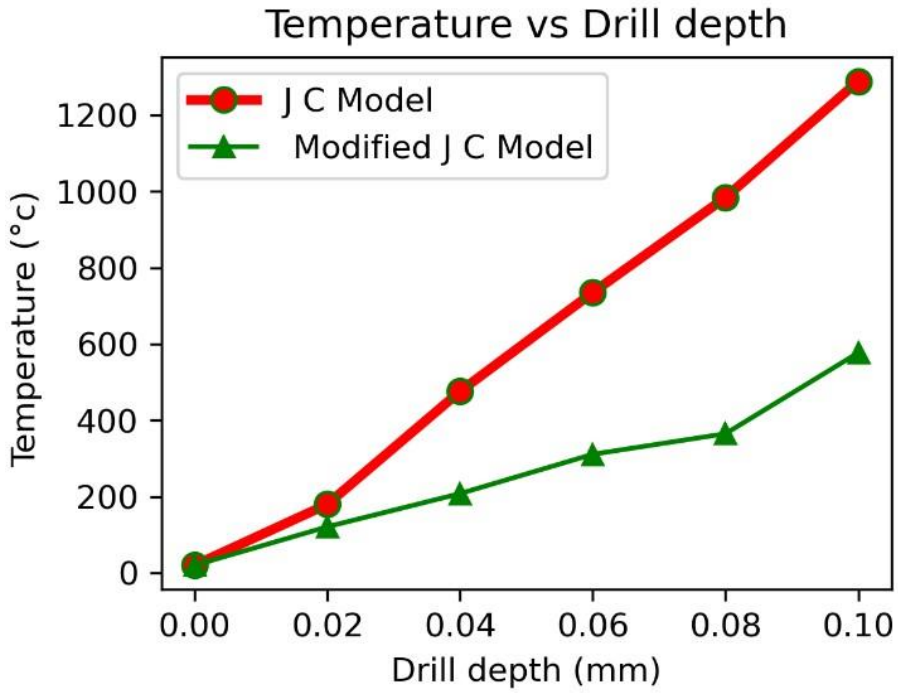

Fig. 4.2: Comparison between J C model and modified J C model of Inconel 625

Fig. 4.2 shows the difference between the J C model and the modified J C model results of temperature for Inconel 625. We can see that the J C model temperature almost reaches the melting point temperature of Inconel 625 at 0.1mm drill depth which is not coherent with real-world values whereas the modified J C model gives acceptable results. These results are obtained by considering specific input parameters such as spindle speed =50krpm and feed rate =3m/min, workpiece diameter = 0.6mm and thickness = 0.1 mm and WC drill bit of 0.3 mm diameter.

Table 4.1: Spindle speed= 50krpm, feed rate= 3m/min:

	Output	Drill depth in (mm)					
		0.00	**0.02**	**0.04**	**0.06**	**0.08**	**0.10**
Workpiece	**Stress (MPa)**	0	1660	1700	1700	1640	1630
	Strain (mm/mm)	0	2.72	3.46	6.07	11.0	16.7
	Strain rate (mm/mm/sec)	0	28400	134000	334000	167000	410000
	Temperature(°C)	20	121	208	311	365	577
Tool	**Interface temperature(°C)**	0	85.4	165	239	297	421
	Sliding velocity(mm/sec)	0	297	547	798	858	975
	Interface pressure (MPa)	0	6140	16400	31800	8820	9780
	Tool wear rate (mm/sec)	0	0	0	0.00000288	0.00000273	0.00000612
	Fz (N)	0	30.3	111	212	173	221

Table 4.2: Spindle speed= 50krpm, feed rate= 4.8m/min:

	Output	Drill depth in (mm)					
		0.00	**0.02**	**0.04**	**0.06**	**0.08**	**0.10**
Workpiece	**Stress (MPa)**	0	1760	1820	1800	1720	1700
	Strain (mm/mm)	0	3.42	4.15	6.78	12.37	18.94
	Strain rate (mm/mm/sec)	0	36500	213000	453000	317000	424000
	Temperature(°C)	20	157	264	356	412	598
Tool	**Interface temperature(°C)**	0	145	234	372	421	624
	Sliding velocity(mm/sec)	0	268	539	734	834	889
	Interface pressure (MPa)	0	7145	17690	42500	10120	12600
	Tool wear rate (mm/sec)	0	0	0	0.00008973	0.00006342	0.0000780
	Fz (N)	0	42.8	124	239	184.8	259.7

Table 4.3: Spindle speed= 80krpm, feed rate= 3m/min:

	Output	Drill depth in (mm)					
		0.00	**0.02**	**0.04**	**0.06**	**0.08**	**0.10**
Workpiece	**Stress (MPa)**	0	1680	1700	1670	1660	1600
	Strain (mm/mm)	0	2.17	3.66	6.40	10.7	13.6
	Strain rate (mm/mm/sec)	0	36400	332000	410000	445000	411000
	Temperature(°C)	20	136	270	402	442	610
Tool	**Interface temperature(°C)**	0	102	204	326	372	475
	Sliding velocity(mm/sec)	0	467	920	1320	1270	1290
	Interface pressure (MPa)	0	5080	9710	15800	7650	8070
	Tool wear rate (mm/sec)	0	0	0	0.00000821	0.00000745	0.0000144
	Fz (N)	0	30.4	118	189	139	144

Table 4.4: Spindle speed= 80krpm, feed rate= 4.8m/min:

	Output	Drill depth in (mm)					
		0.00	**0.02**	**0.04**	**0.06**	**0.08**	**0.10**
Workpiece	**Stress (MPa)**	0	1764	1880	1820	1700	1730
	Strain (mm/mm)	0	4.21	5.34	8.83	12.78	16.67
	Strain rate (mm/mm/sec)	0	43200	498000	513000	467000	423000
	Temperature(°C)	20	157	327	565	621	723
Tool	**Interface temperature (°C)**	0	149	278	445	498	599
	Sliding velocity(mm/sec)	0	314	886	1289	1163	1078
	Interface pressure (MPa)	0	6134	9914	17880	9840	9970
	Tool wear rate (mm/sec)	0	0	0.0000067	0.0000189	0.0000238	0.0000945
	Fz (N)	0	43.7	136	213	178	164

Table 4.5: Spindle speed= 140krpm, feed rate= 3m/min:

	Output	Drill depth in (mm)					
		0.00	**0.02**	**0.04**	**0.06**	**0.08**	**0.10**
Workpiece	**Stress (MPa)**	0	1674	1700	1640	1620	1600
	Strain (mm/mm)	0	2.97	4.95	8.39	12.0	17.6
	Strain rate (mm/mm/sec)	0	645000	706000	1130000	653000	621000
	Temperature(°C)	20	194	351	484	513	756
Tool	**Interface temperature(°C)**	0	146	295	430	464	514
	Sliding velocity(mm/sec)	0	1287	1630	2210	2260	2436
	Interface pressure (MPa)	0	4390	7800	7000	5950	6350
	Tool wear rate (mm/sec)	0	0	0.00000370	0.0000252	0.0000287	0.0000312
	Fz (N)	0	79	118	124	94	105

Table 4.6: Spindle speed= 140krpm, feed rate= 4.8m/min:

	Output	Drill depth in (mm)					
		0.00	**0.02**	**0.04**	**0.06**	**0.08**	**0.10**
Workpiece	**Stress (MPa)**	0	1680	1700	1670	1660	1640
	Strain (mm/mm)	0	3.97	5.78	9.67	14.87	19.76
	Strain rate (mm/mm/sec)	0	713000	765000	1240000	798000	723000
	Temperature(°C)	20	228	415	548	617	821
Tool	**Interface temperature(°C)**	0	158	345	465	497	569
	Sliding velocity(mm/sec)	0	1137	1580	2170	2240	2380
	Interface pressure (MPa)	0	4780	8160	7980	6440	6670
	Tool wear rate (mm/sec)	0	0	0.0000078	0.0000249	0.0000475	0.0000870
	Fz (N)	0	91	128	159	164	147

Table. 4.1 to Table 4.6 shows the simulation results for different spindle speeds with the corresponding feed rates. The results are in the form of stress, strain, strain rate, temperature for the workpiece and interface temperature, sliding velocity, interface pressure, and tool wear rate for the tool respectively. It should be noted that only maximum values are shown in the tables and F_z = axial thrust on the tool.

The following simulation results are evaluated at different drill depths for a spindle speed of 80krpm and feed rate of 3m/min. Results are considered according to local conditions (w.r.t drill depth).

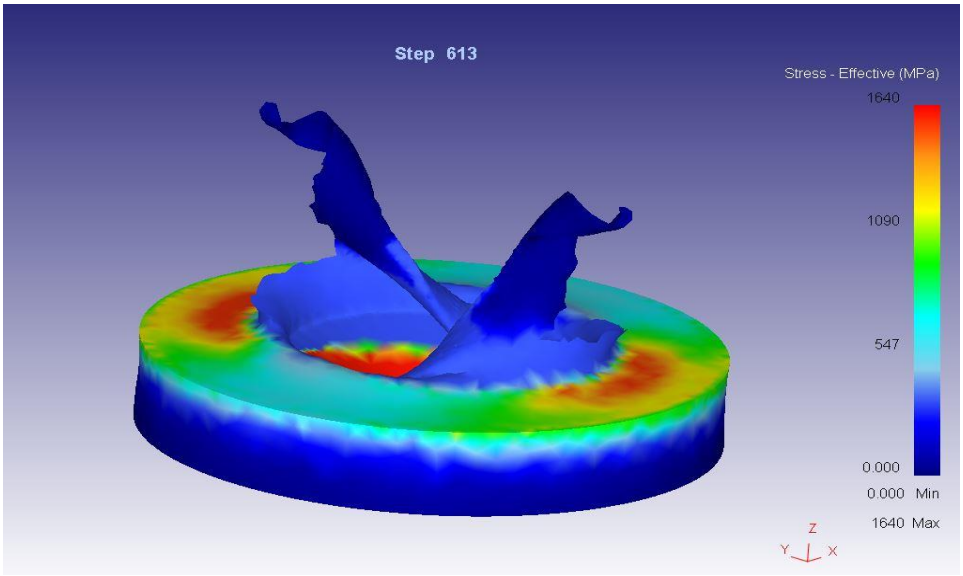

Fig. 4.3: Stress condition of work piece at a drill depth of 0.08mm

Fig. 4.3 shows stress condition of the workpiece when the micro-drill bit has reached the depth of 0.08mm along the (-ve) Z direction. At this stage maximum stress values are observed in centre region and at the contact between workpiece and cutting edge of the tool.

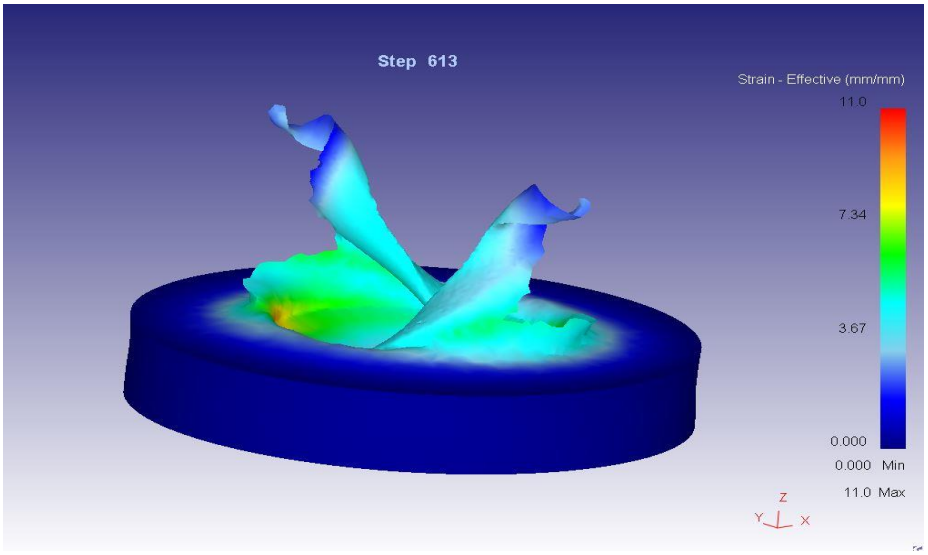

Fig. 4.4: Strain condition of work piece at a drill depth of 0.08mm

Fig. 4.4 shows strain condition of the workpiece when the micro-drill bit has reached the depth of 0.08mm along the (-ve) Z direction. At this stage, highest strain value is observed at the contact between cutting-edge of the tool and workpiece which is shown in red colour.

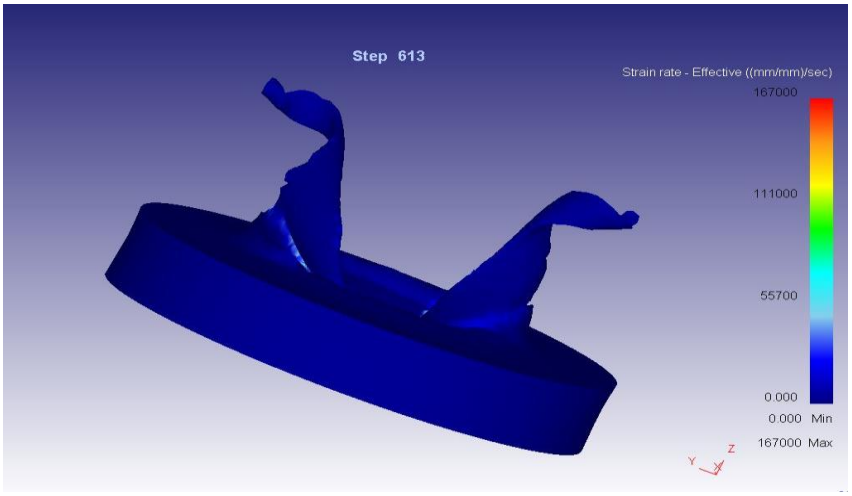

Fig. 4.5: Strain rate condition of work piece at a drill depth of 0.08mm

Fig. 4.5 shows the strain rate condition of the workpiece when the micro-drill bit has reached the depth of 0.08mm along the (-ve) Z direction. The unit of strain rate is s^{-1}. No variation is observed at this stage which is shown in blue colour which is minimum.

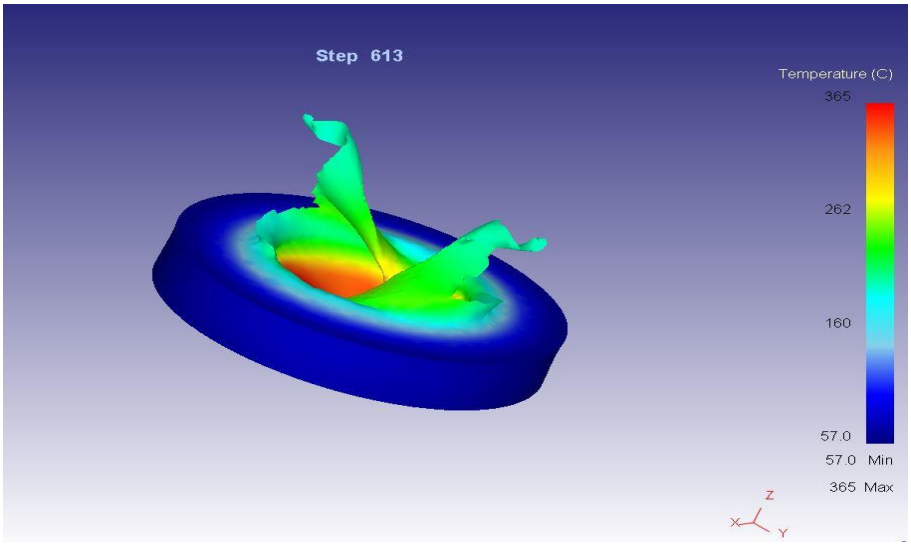

Fig. 4.6: Temperature condition of work piece at a drill depth of 0.08mm

Fig. 4.6 shows temperature condition of the workpiece when the micro-drill bit has reached the depth of 0.08mm along the (-ve) Z direction. At this stage, centre portion of the workpiece is having high temperature shown in red colour and the temperature is decreased radially from the centre. Due to large difference in temperature value between at the centre and at the surrounding which indicates that Inconel 625 material has low thermal conductivity.

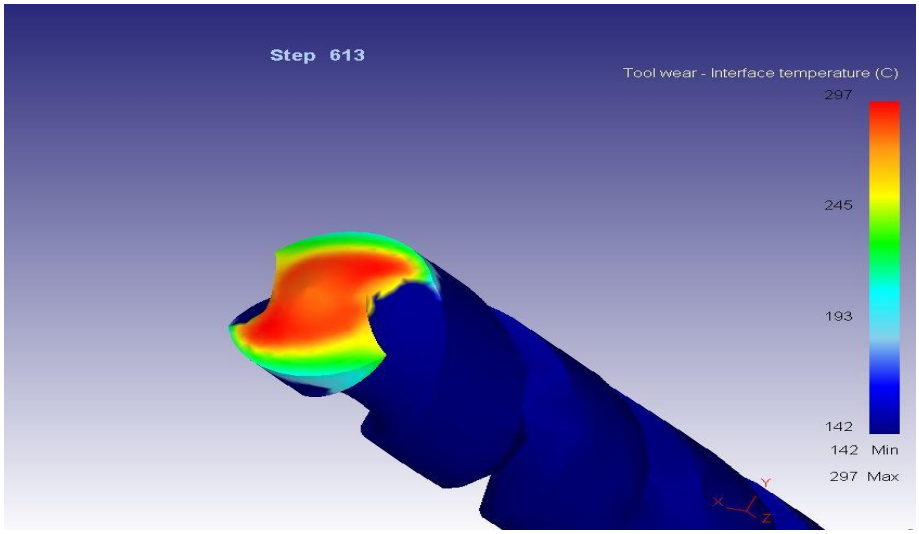

Fig. 4.7: Interface temperature at drill depth 0.08mm

Fig. 4.7 shows the interface temperature of the tool when penetrates the workpiece up to 0.08mm thickness. At this stage the tool's core region is shown in red colour which is having highest temperature because of adiabatic heating occurring inside the workpiece.

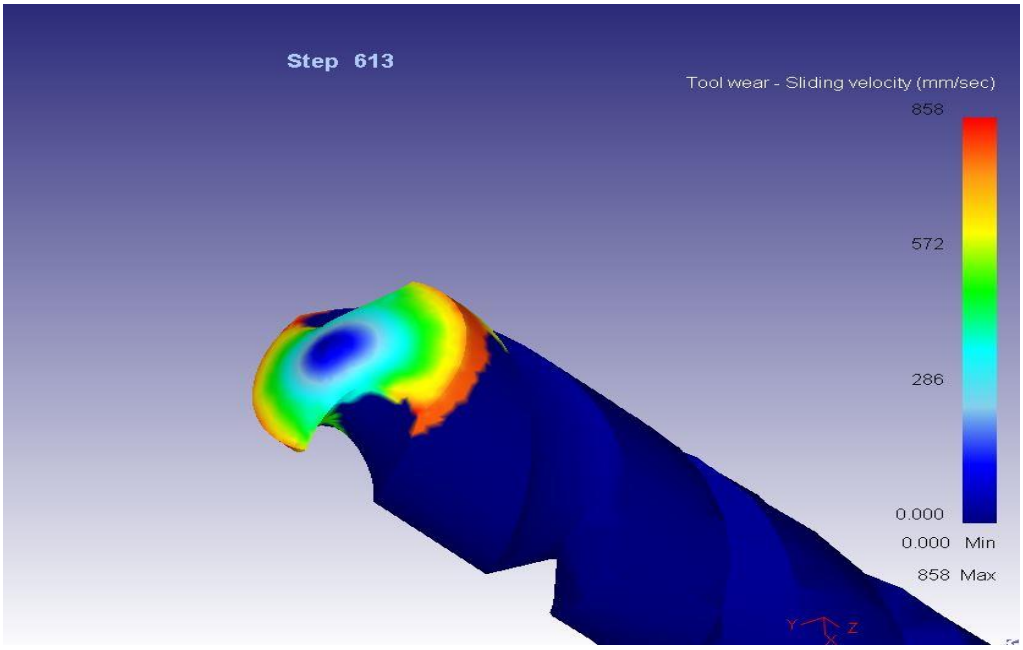

Fig. 4.8: Sliding Velocity at drill depth 0.08mm

Fig. 4.8 shows the sliding velocity of the tool when penetrates the workpiece up to 0.08mm thickness. At this stage, sliding velocity is maximum at the outer region of the tool which is indicated in red colour and at the inner core region it shows minimum value which is indicated in blue colour.

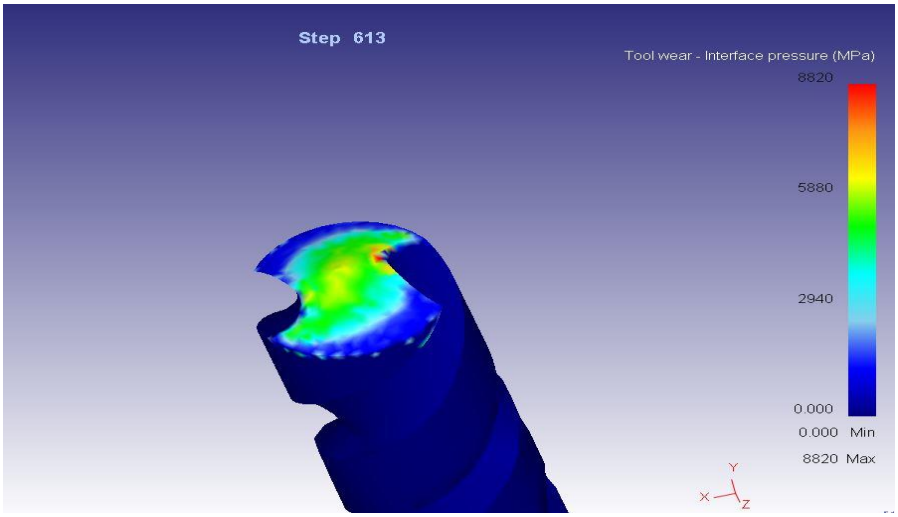

Fig. 4.9: Interface pressure at drill depth 0.08mm

Fig. 4.9 shows the interface pressure of the tool when penetrates the workpiece up to 0.08mm thickness. At this stage, the cutting-edge region has the highest interface pressure with red colour spots shown in red and yellow colours and the remaining regions indicated in green and blue colours show low pressure.

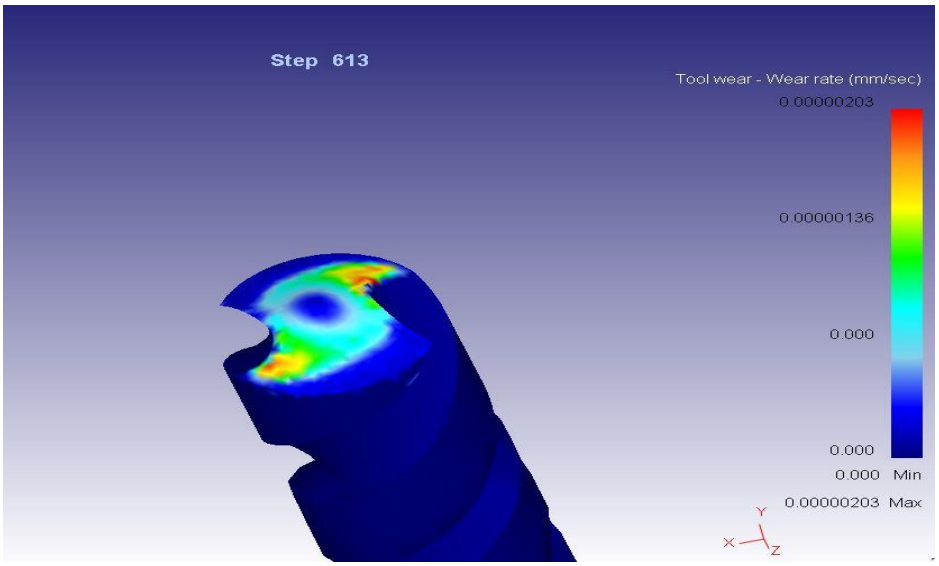

Fig. 4.10: Tool wear rate at drill depth 0.08mm

Fig. 4.10 shows wear rate of the tool when penetrates the workpiece up to 0.08mm thickness. At this stage, the tool wear rate is zero with in centre of the micro-drill bit. However, we can see red spots near the cutting-edge areas, which shows the high wear rate.

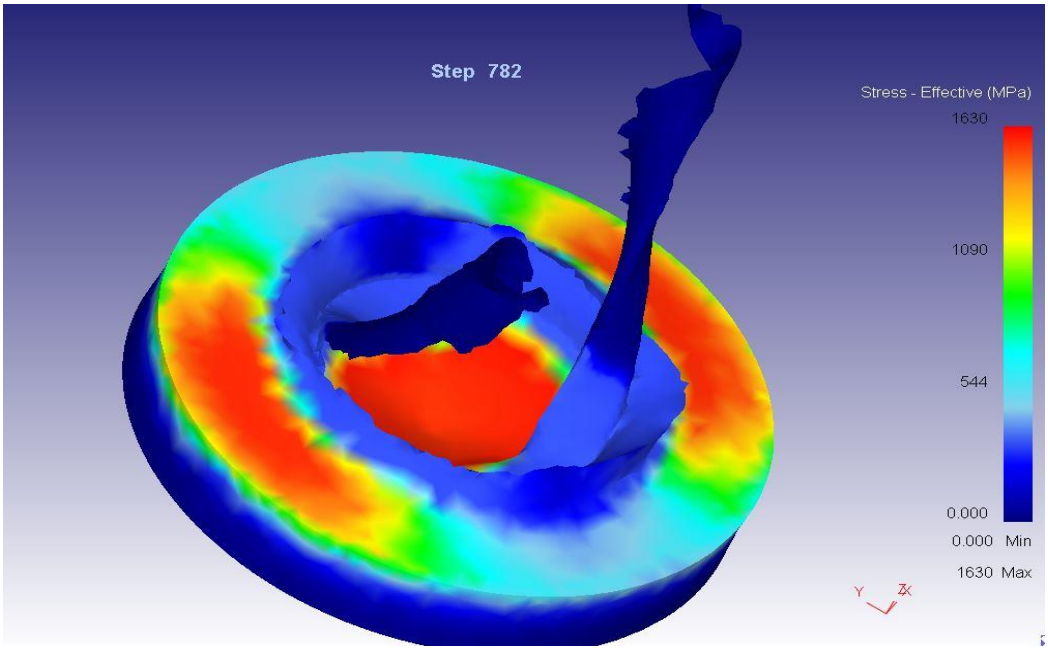

Fig. 4.11: Stress condition of work piece at a drill depth of 0.10mm

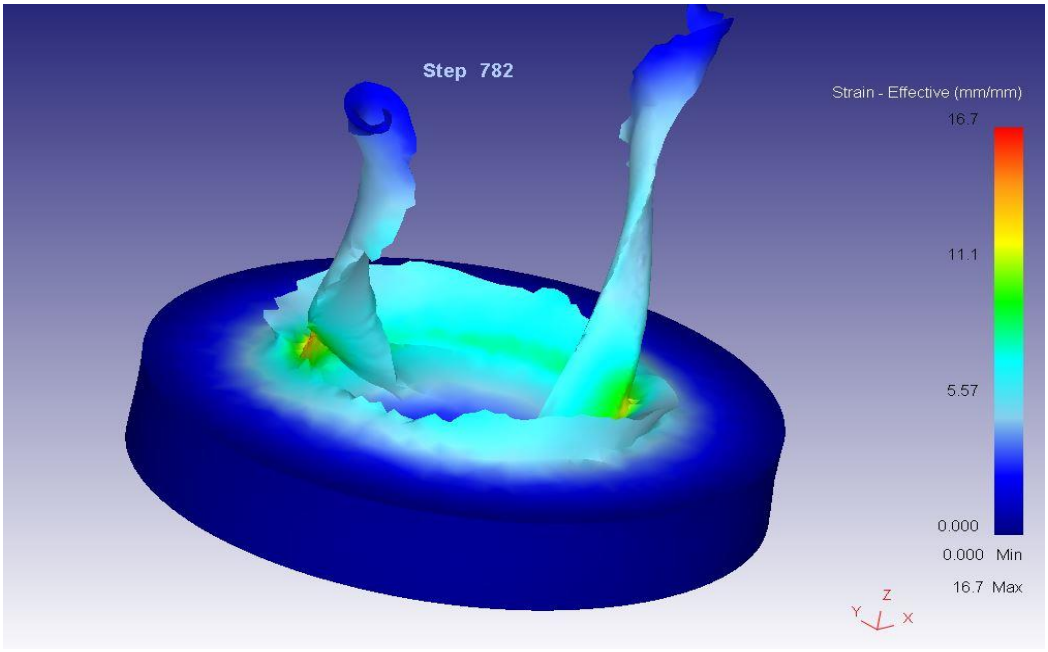

Fig. 4.12: Strain condition of work piece at a drill depth of 0.10mm

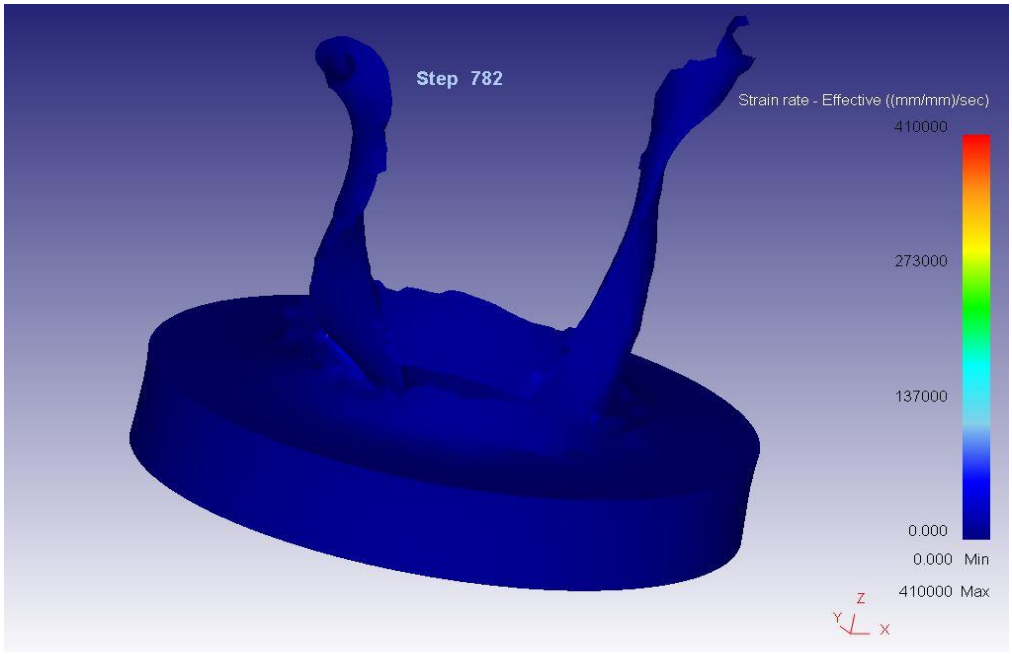

Fig. 4.13: Strain rate condition of work piece at a drill depth of 0.10mm

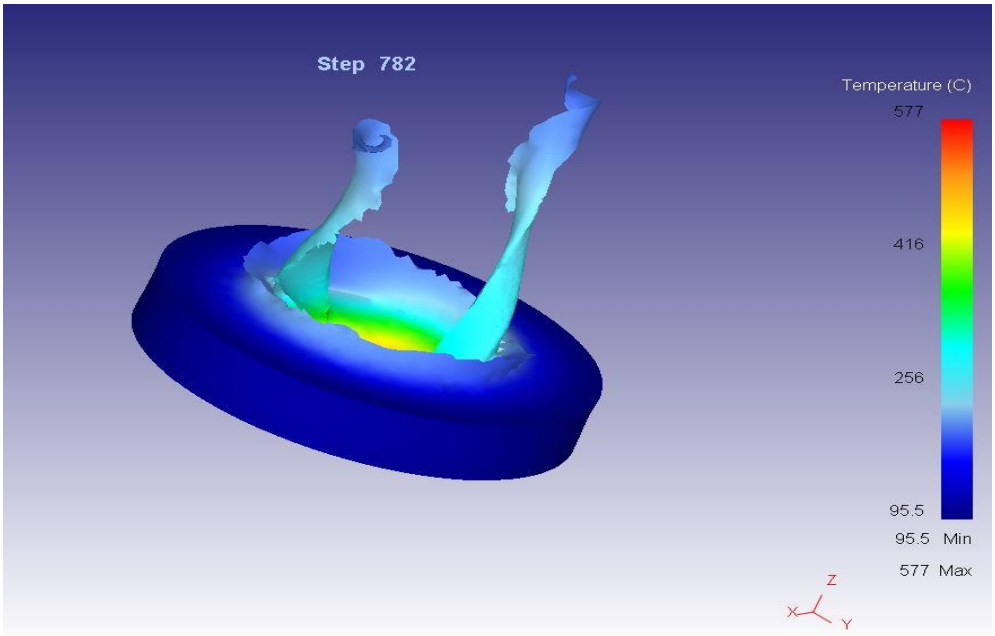

Fig. 4.14: Temperature condition of work piece at a drill depth of 0.10mm

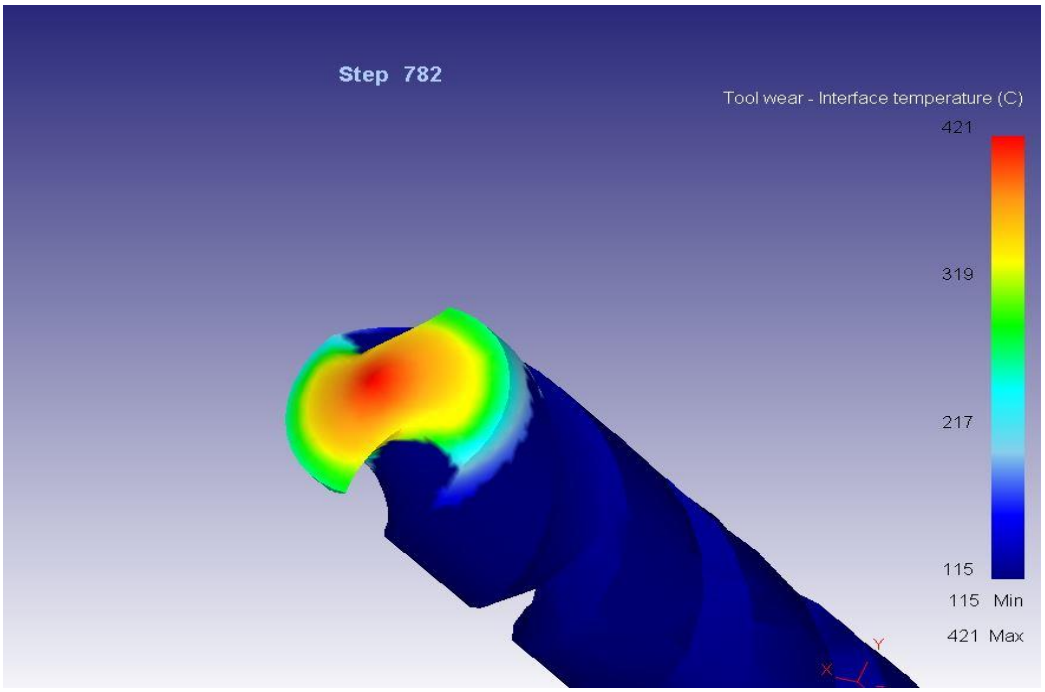

Fig. 4.15: Interface temperature at drill depth 0.10mm

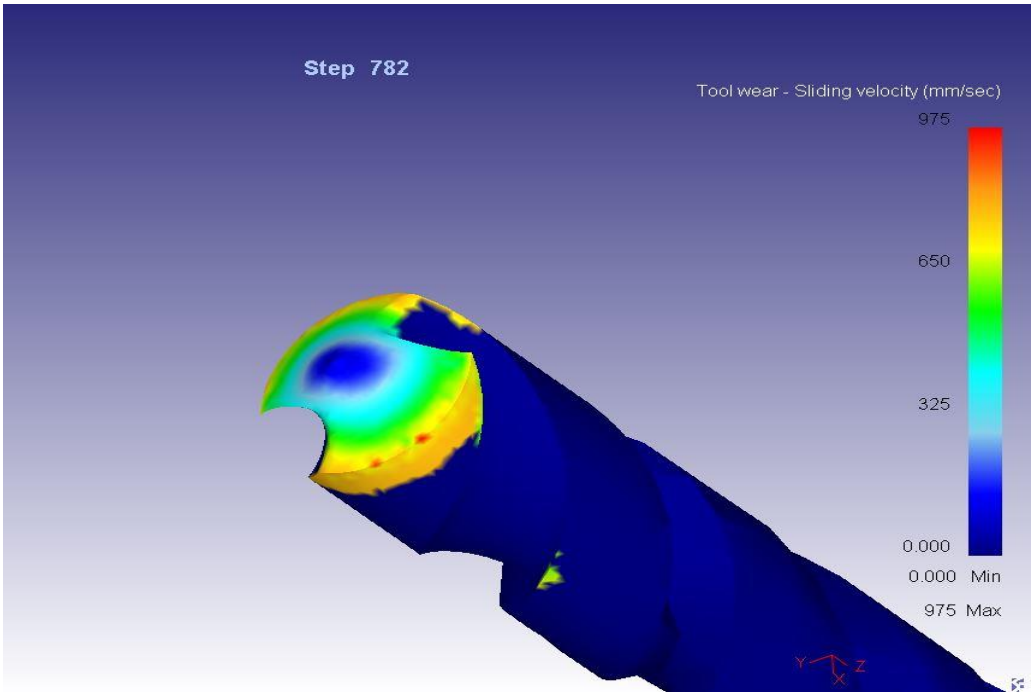

Fig. 4.16: Sliding Velocity at drill depth 0.10mm

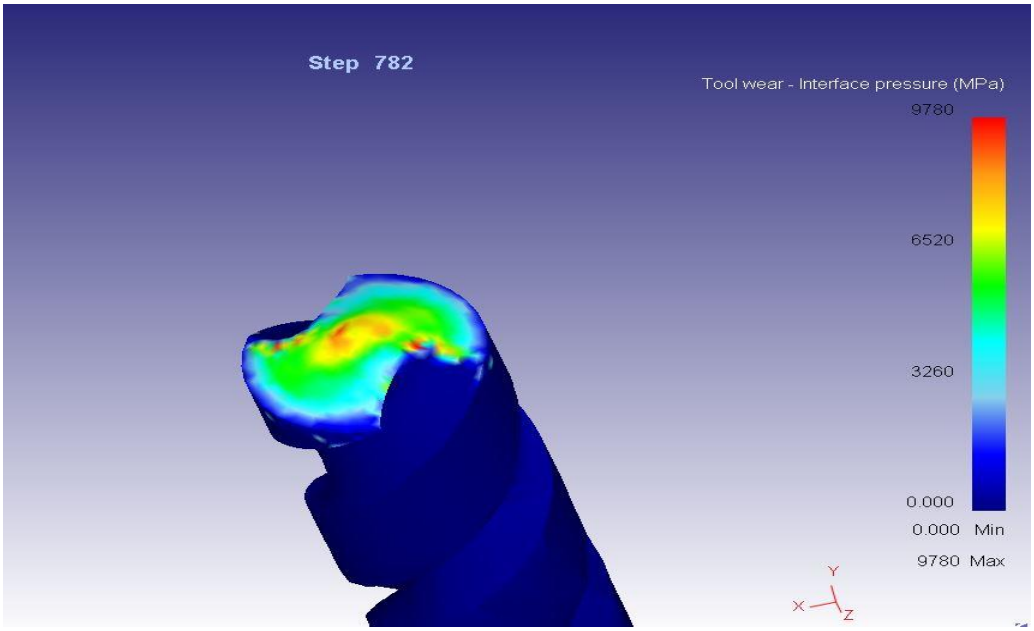

Fig. 4.17: Interface pressure at drill depth 0.10mm

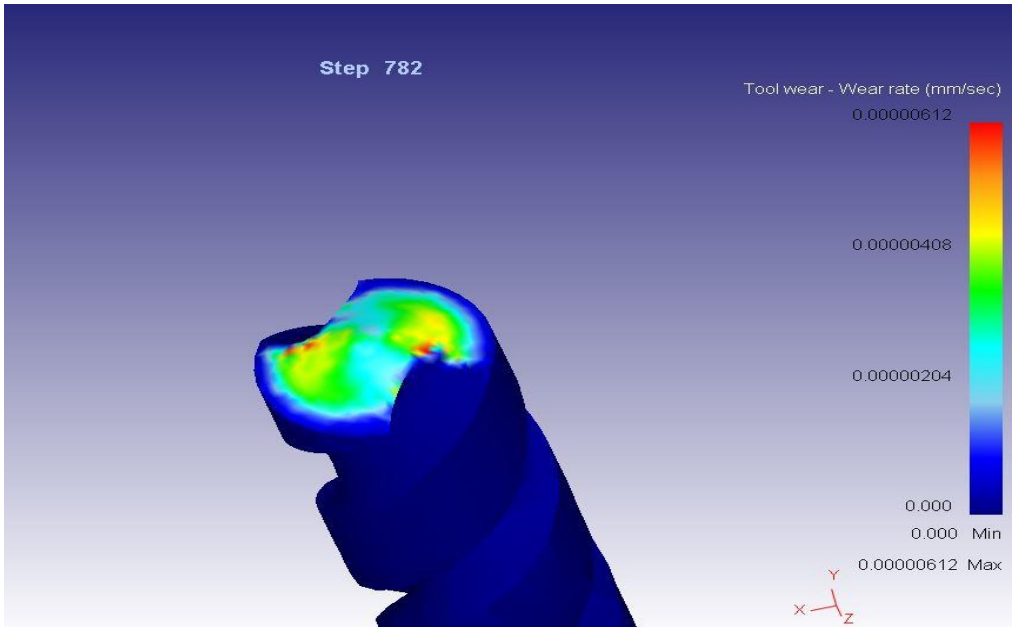

Fig. 4.18: Tool Wear rate at drill depth 0.10mm

Fig. 4.11 to Fig. 4.18 shows similar results with respect to drill depth of 0.08mm condition

For 50krpm - 4.8m/min, 80krpm - 3m/min, 80krpm - 4.8m/min, 140krpm - 3m/min, 140krpm - 4.8m/min simulation, the results are almost similar by having different values.

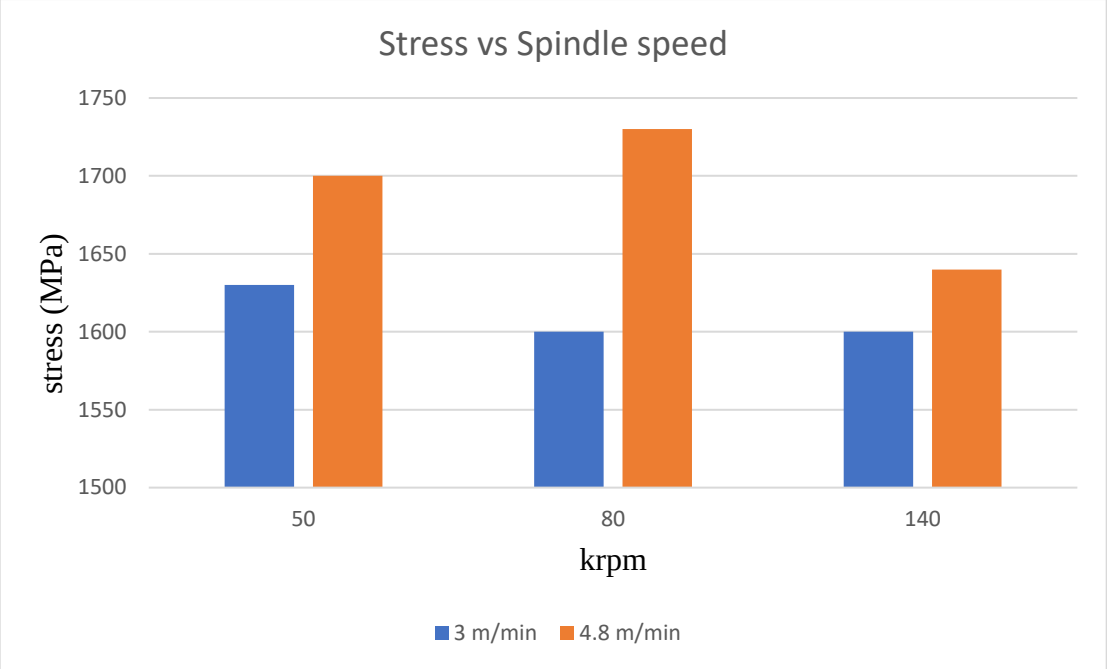

Fig. 4.19: Comparison between Stress and Spindle speed with different feed rates

Fig. 4.19 shows that the decrease in stress for 3m/min feed rate with increase in spindle speeds. But when feed rate is 4.8m/min the stress value is decreased at 140krpm compare to the 50krpm, 80krpm.

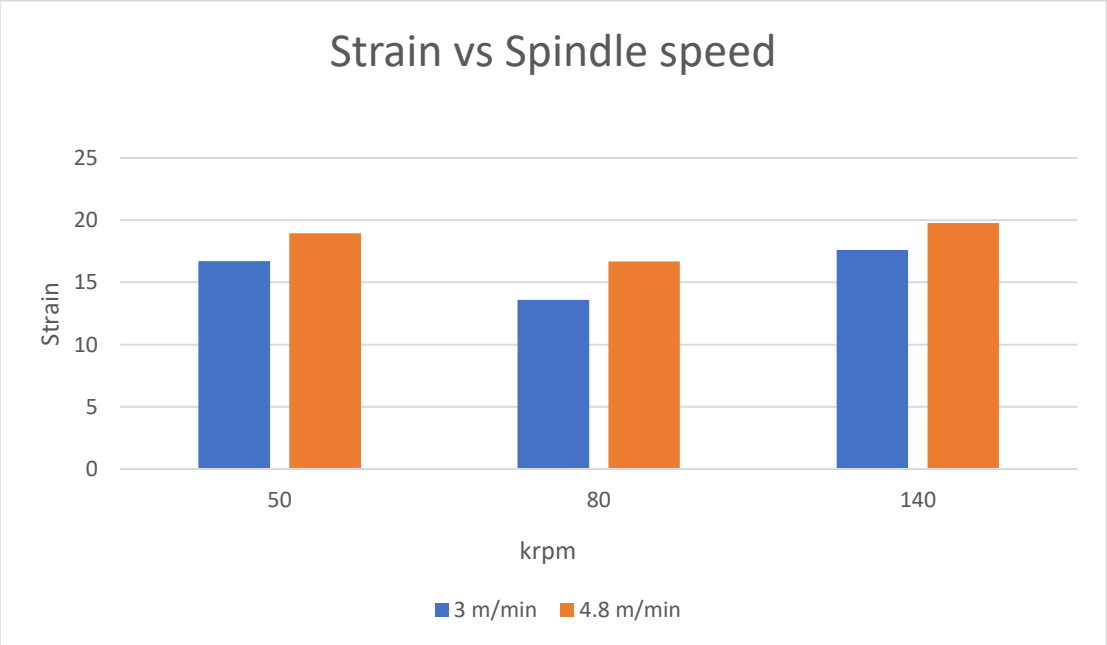

Fig. 4.20: Comparison between Strain and Spindle speeds with different feed rates

Fig. 4.20 shows that the strain value is lower at 80krpm than it is at 50krpm with the corresponding feed rates.

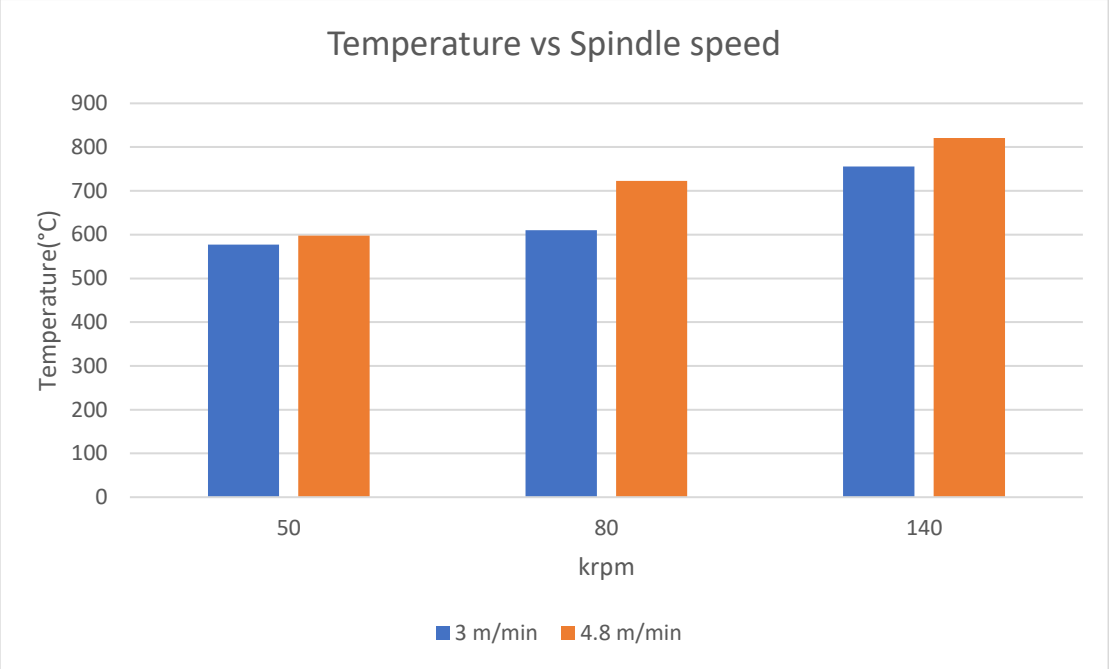

Fig. 4.21: Comparison between Temperature and Spindle speeds with different feed rates

Fig. 4.21 shows that there is an increase in temperature with increase in spindle speed and feed rates.

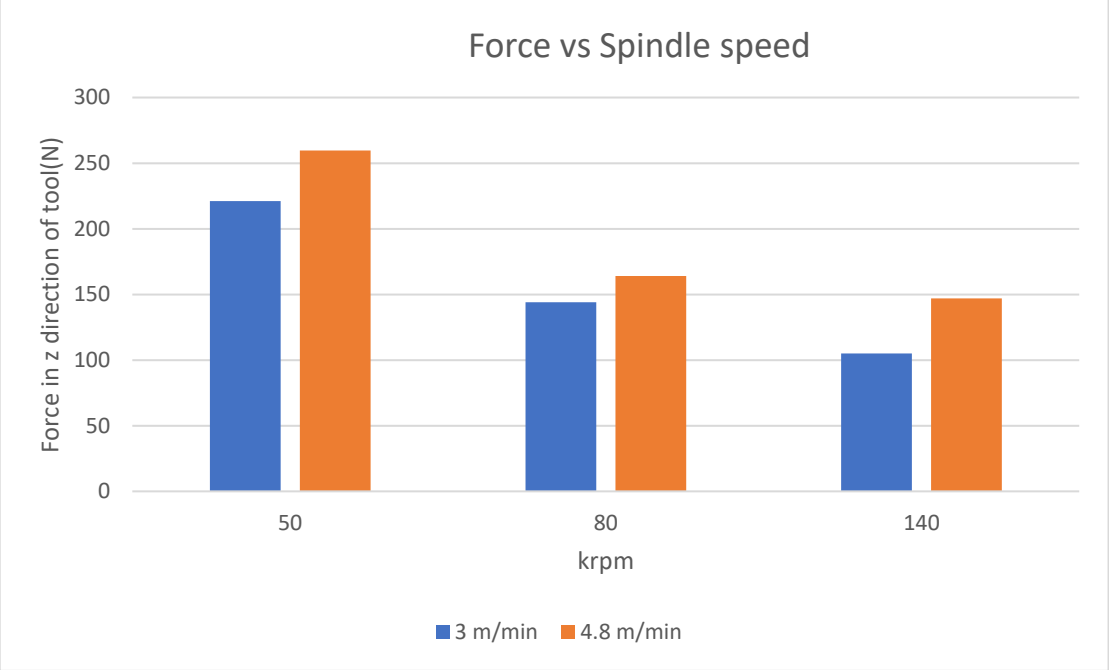

Fig. 4.22: Comparison between Force and Spindle speeds with different feed rates

Fig. 4.22 shows that the axial thrust on the tool continues to decrease as spindle speed rises.

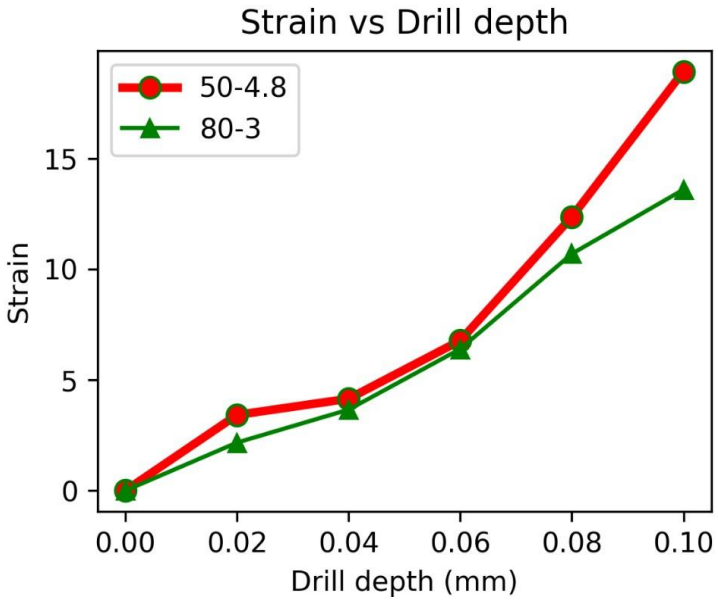

Fig. 4.23: Graph between strain and drill depth. (50-4.8)- 50krpm and 4.8m/min, (80-3)- 80krpm and 3 m/min.

Fig. 4.23 shows that the strain values are parallel for both the conditions for drill depths ranging from 0.04-0.06mm. Additionally, the 50krpm-4.8m/min has a steeper slope for remaining drill depths than the 80krpm-3m/min.

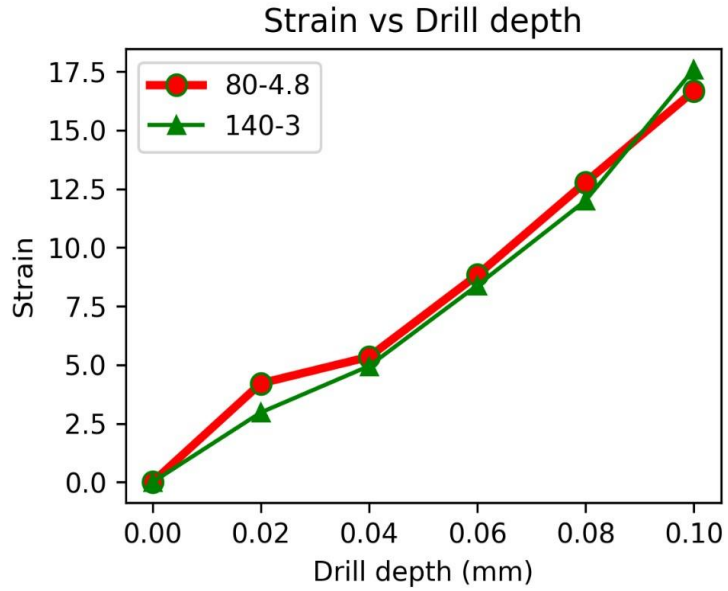

Fig. 4.24: Graph between strain and drill depth. (80-4.8)- 80krpm and 4.8m/min, (140-3)- 140krpm and 3 m/min

.

Fig. 4.24 shows the strain levels for both circumstances are approximately parallel. However, the strain for 80krpm-4.8m/min has a steeper slope at drill depths of 0.02mm.

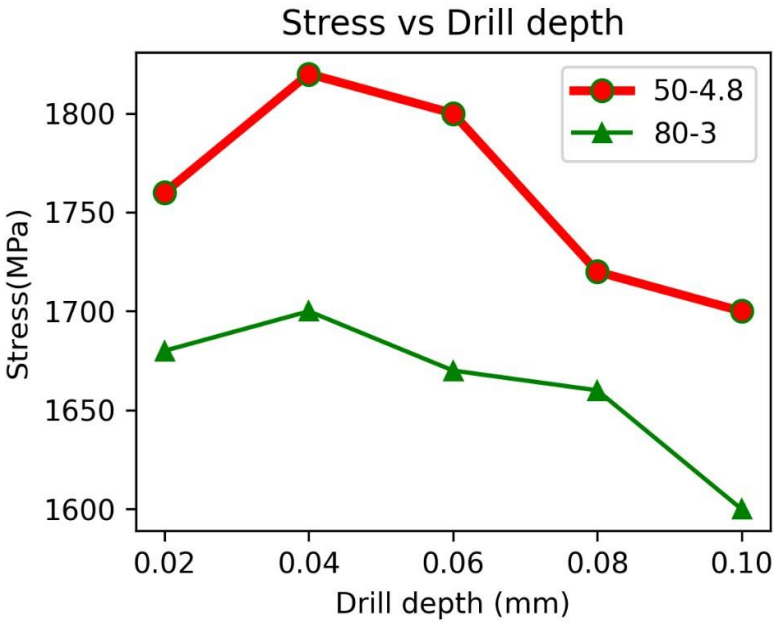

Fig. 4.25: Graph between stress and drill depth. (50-4.8)- 50krpm and 4.8m/min, (80-3)- 80krpm and 3 m/min.

Fig. 4.25 shows rapid decrease in stress value from 0.04-0.06mm drill depth for 50krpm-4.8m/min and gradual decrease for 80krpm-3m/min. we can also observe rapid decrease stress from 0.08mm drill depth for 80krpm-3m/min.

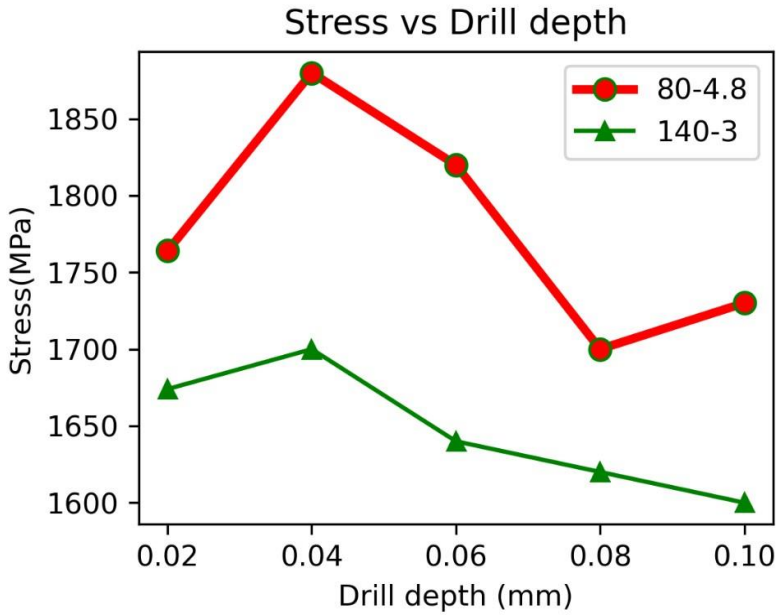

Fig. 4.26: Graph between stress and drill depth. (80-4.8)- 80krpm and 4.8m/min, (140-3)- 140krpm and 3 m/min.

Fig. 4.26 shows that for both conditions the value of stress increased for drill depth between 0.02-0.04mm. After that, the value of stress starts to decline at drill depths

between 0.04-0.08mm. But we can observe increase in value of stress for 80krpm-4.8m/min from 0.08-mm drill depth.

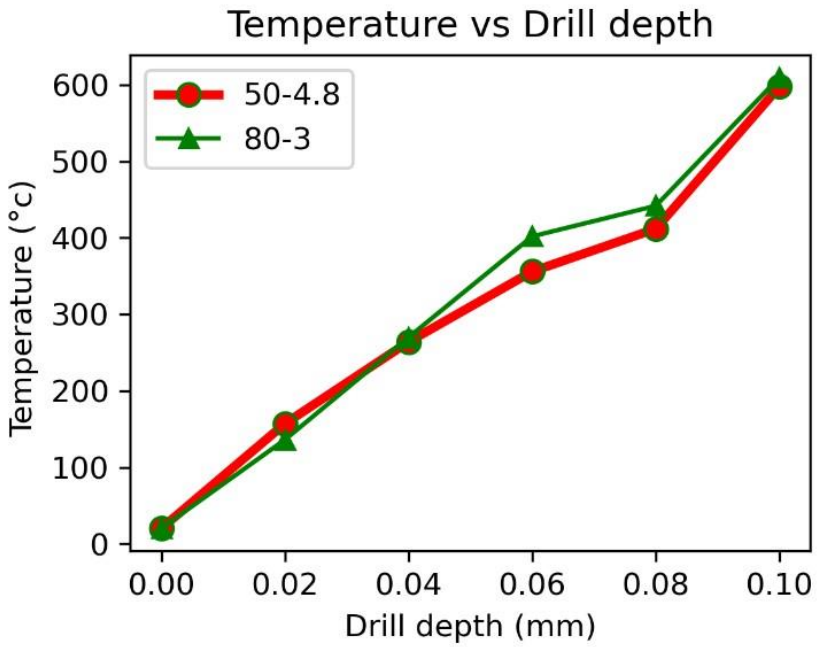

Fig. 4.27: Graph between temperature in (°c) and drill depth. (50-4.8)- 50krpm and 4.8m/min, (80-3)- 80krpm and 3 m/min.

Fig. 4.27 shows parallel slopes for both the conditions but there is increase in slope for 50krpm-4.8m/min at a drill depth of 0.06mm.

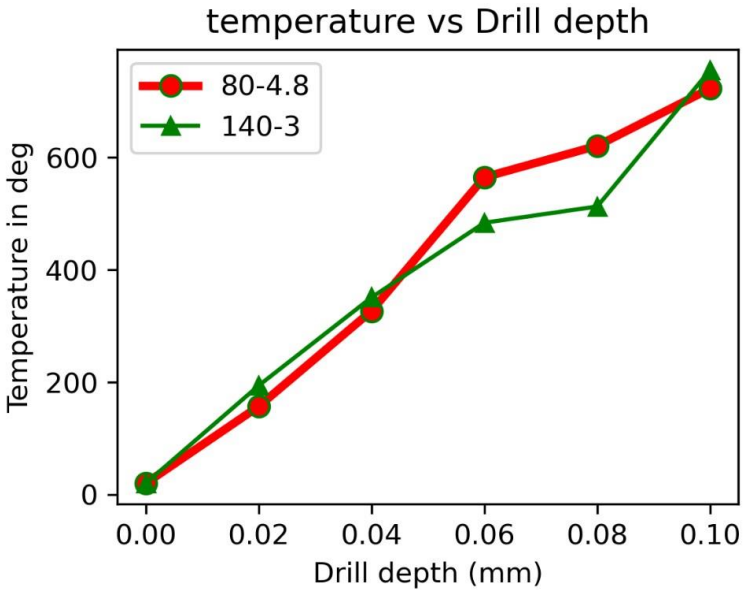

Fig. 4.28: Graph between Temperature in (°c) and drill depth. (80-4.8)- 80krpm and 4.8m/min, (140-3)- 140krpm and 3 m/min.

Fig. 4.29 shows parallel slopes for both the conditions up to the drill depth of 0.04mm and we can observe the deviation in slopes for drill depth ranging from 0.04-0.1mm

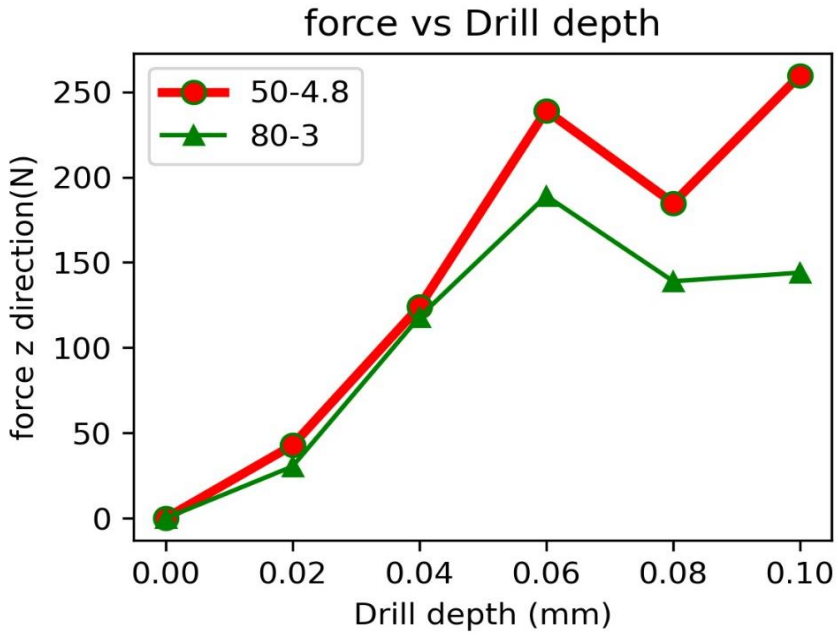

Fig. 4.30: Graph between Force and drill depth. (50-4.8)- 50krpm and 4.8m/min, (80-3)- 80krpm and 3 m/min.

Fig. 4.30 shows that for both conditions, the slopes are parallel up to a drill depth of 0.04 mm. Additionally, the slope for both situations decreases at drill depths between 0.06 and 0.08 mm. Following a drill depth of 0.08mm at 50krpm-4.8m/min, the slope suddenly increases.

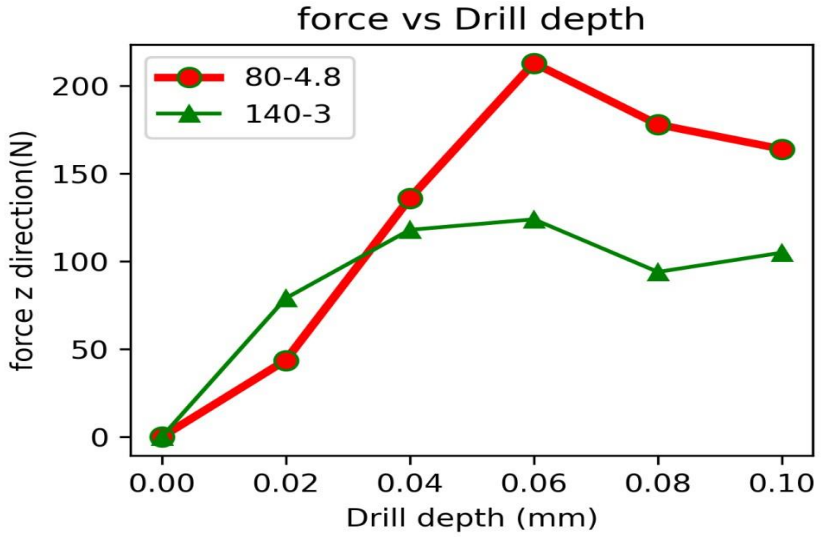

Fig. 4.31: Graph between Force and drill depth. (80-4.8)- 80krpm and 4.8m/min, (140-3)- 140krpm and 3 m/min.

Fig. 4.32 shows increase in slope for both the conditions up to the drill depth of 0.06mm. And after that we observe decrease in force on the tool. But for 140krpm-3m/min condition we can observe the increase in slope from 0.08mm drill depth.

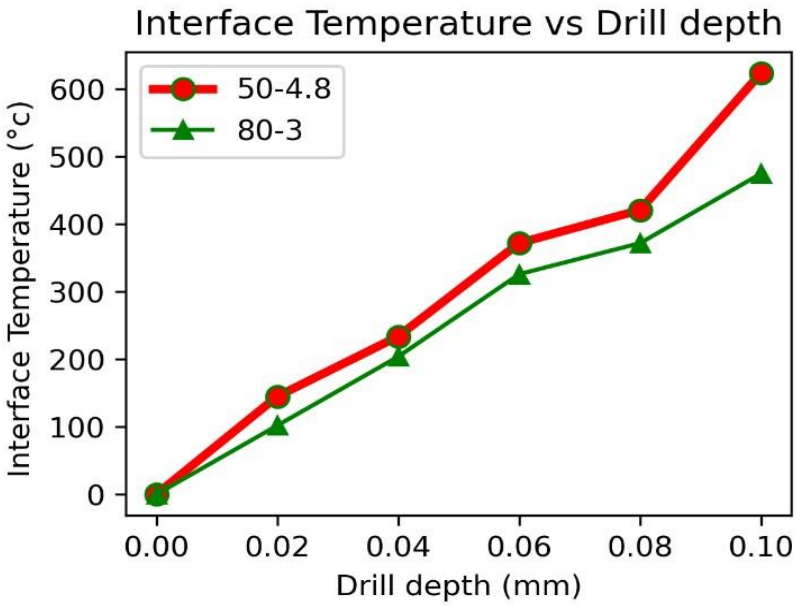

Fig. 4.33: Graph between Interface temperature in (°c) and drill depth. (50-4.8)- 50krpm and 4.8m/min, (80-3)- 80krpm and 3 m/min.

Fig. 4.33 shows that up to the drill depth of 0.08 mm, there is little difference in the interface temperature readings for the two conditions, but after that the we can observe the increase in slope for 50 krpm-4.8 m/min.

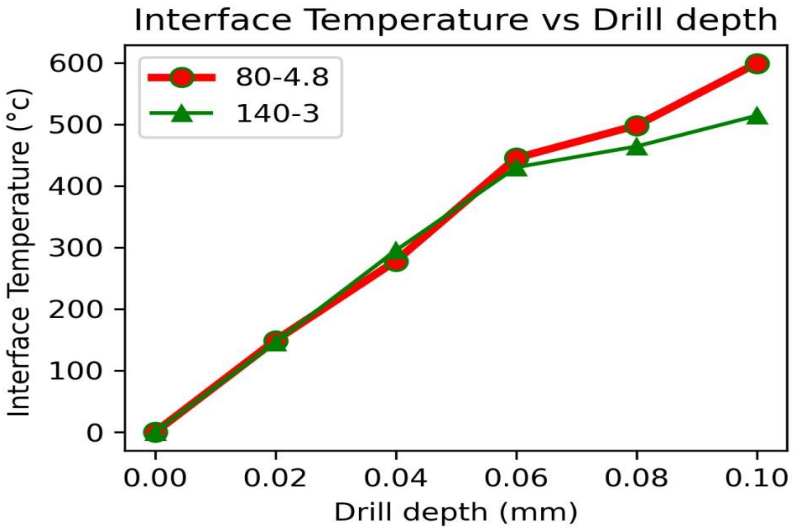

Fig. 4.34: Graph between Interface temperature in (°c) and drill depth. (80-4.8)- 80krpm and 4.8m/min, (140-3)- 140krpm and 3 m/min.

Fig. 4.34 shows that the slopes for the two conditions were nearly same up to the drill depth of 0.06mm, but after that interface temperature values varied.

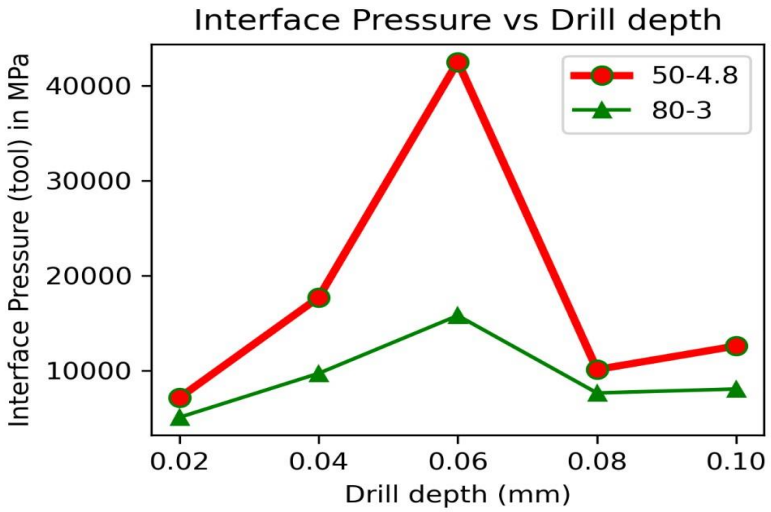

Fig. 4.35: Graph between Interface pressure and drill depth. (50-4.8)- 50krpm and 4.8m/min, (80-3)- 80krpm and 3 m/min.

Fig. 4.35 shows similar plot diagrams for both the conditions but there is a greater amount of variation in interface temperature at drill depth of 0.06mm for 50krpm-4.8m/min.

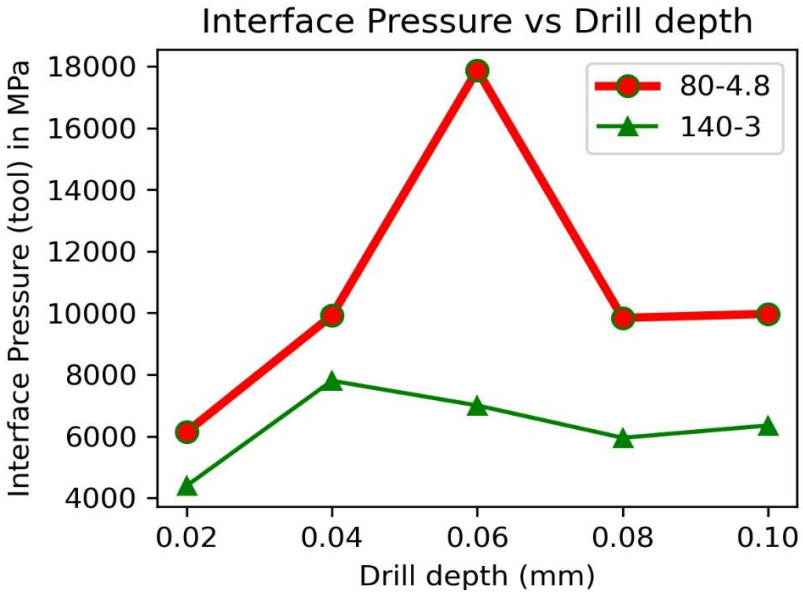

Fig. 4.36: Graph between Interface pressure and drill depth. (80-4.8)- 80krpm and 4.8m/min, (140-3)- 140krpm and 3 m/min.

Fig. 4.36 shows sudden variation in interface pressure for 80krpm-4.8m/min and a gradual decrease in slope for 140krpm-3m/min when drill depth ranges from 0.04-0.08mm.

5. CONCLUSION

1) The main cause of the rise in temperature, stress, etc., is the impact of feed rate.

2) The material model is crucial to the simulation process.

3) Due to adiabatic heating, increasing spindle speeds cause the temperature to rise and axial force on the tool to decrease.

4) The modified Johnson-Cook model gives acceptable results compared to the normal Johnson-Cook model.

6. LIMITATIONS

1) The size of the micro drill bit has a direct impact on the size of the workpiece. The size of the workpiece should be 20% to 50% larger than the size of the micro drill bit for chip removal. Additionally, the rpm for chip removal should be high.

2) Due to tool translational motion, the entire deformed material moves along the -ve Z direction if the Velocity boundary condition of the workpiece is not fixed in the Z direction.

3) We cannot notice the burr formation on the exit side if the workpiece's velocity boundary condition is fixed in the Z direction.

4) Large-sized workpieces can make adaptive meshing difficult. And the material removal from the workpiece is not visible to us.

5) If we select an elastic or elastoplastic material type, the simulation will take longer to run and chip removal will be more challenging.

6) Since Deform3D is primarily used to calculate values for stress, strain, temperature, and strain rate, we cannot expect the hole quality.

7) Simulated objects are thought to be made of the ideal material, free of any strain-hardening elements or residual stresses.

7. FUTURE WORK

1) If the simulation work's results coincide with those of the experiment, we can use the simulation technique by changing the parameters, which is safer than the actual work and less expensive.

2) Deform 3D software needs to be improved to detect chips in huge workpieces for the micro-drilling process.

8. REFERENCES

1. Geddes B, Leon H, Huang X, “Superalloys: alloying and performance”. ASM International (2010).

2. Report Nickel Superalloy Market (2020), Global Market Insights, Delaware, USA

3. Sims CT, “High-temperature materials for aerospace and industrial power (1987), New York”. ISBN: 0-471-01147-9.

4. Ross EW, Sims CT, “High-temperature materials for aerospace and industrial power” (1987)

5. Jung Bahadur Singh, “Alloy 625 Microstructure, properties and performance” (2022) ISBN 978-981-19-1561-1 https://doi.org/10.1007/978-981-19-1562-8

6. Eiselstein HL, Tillacj DJ, “The invention and definition of alloy 625” (1991).

7. Koepfer, C., “Micro-Drilling: some questions to think About, in production Machining” (2009).

8. Zhuang, Y., “Optimizing the Economic Efficiency by Micro drill life improvement during Deep Hole Drilling in the 212 Valve Manufacturing Process” (2013).

9.Szalay, T., K. Patra and B.Z. Farkas, “Experimental investigation of tool breakage in micro-drilling of EN AW-5083 Aluminium”. Key Engineering Materials (2013).

10. Kudla, L., “Limitations of Mechanical Micro-Drilling in Difficult-to-machine materials”. In Proceedings of the 12th euspen International Conference (2012).

11. Kudla L., “Experimental research of cutting forces in Micro drilling”. In Proceedings of the euspen International Conference (2011).

12. Kudla L., “Investigation into micromachining techniques applied for improvement of the geometry of micro drills”. In proceedings of 3rd international conference high-performance cutting (2008).

13. Kudla L., “Prevention against breakage of miniature drills”. Mechanical engineering (2006).

14. Nair, M.H, “Improving the sequential mechanical micro-drilling of Inconel 718 alloy” (2012).

15. Kudla L., “Progress in fabrication of Smallest Micro drills”. In proceedings of the 11th International Conference Inter-Academia (2012).

16. Egashire, k. and k. Mizutani, “Micro drilling of monocrystalline silicon using a cutting tool”. Precision Engineering-journal of the international Societies for Precision Engineering and Nano technology(2002).

17. Lee, A.C., et al., “Design of a new micro single flute drill. Energy development” (2014).
18. Liang, X., et. al, “Mechanical drilling of PCB micro-hole and its application in micro ultrasonic powder moulding”(2015).
19. Aziz, M., O. Ohnishi, and H. Onikura, “Innovative micro hole machining with minimum burr formation by the use of the newly developed micro compound tool”(2012).
20. Hasan, Mahadi; Zhao, Jingwei; and Jiang Zhengyi, “A review of modern advancements in micro drilling techniques”(2017).
21. Friedrich, D.C, “Precision Micromanufacturing process” http://www.me.mtu.edu/~microweb/chap6/ch6-0.htm
22. Egashire, K. and K. Mizutani, “Milling using ultra-small diameter ball end mills fabricated by electrical discharge machining. Journal -Japan Society for Precision Engineering” (2003)
23.
24. E.J.A. Armarego, “Some fundamental and principal aspects of twist drills and drilling” (1994).
25. C.J. Oxford, “On the drilling of metals 1 – basic mechanics of the process”, ASME, 1995.
26. E.J.A. Armarego, “Some fundamental and principal aspects of twist drills and drilling” (1994).
27. D.F. Galloway, “Some experiments on the influence of various factors on drill performance” (1957).
28. M. S. Cheong. D. W. cho, K.F. Ehmann, “Identification and control for micro drilling productivity enhancement” (1999).
29. M.C. Shaw, “metal cutting principles”, 2nd Edition, Oxford University Press, Inc, NewYork, 2005.
30. G. Spur, J.R. Masuha, “Drilling with twist drills of different cross-section profiles”, CIRP Annals-Manufacturing Technology (1981).
31. J.S Agapiou, D.A. Stephenson, “Analytical and experimental studies of drill temperature”(1994).
32. M.C. Shaw and C. J.J. Oxford, “on the drilling of metals-2 the torque and thrust in drilling” (1957).
33. M. kronenberg, Grundzuge der zerpanungslehre springer verlag, Berlin (1963).

34. S. Muthukrishna, S.V., C. Sujatha, “Twist drill deformation and optimum drill geometry” (1994).
35. W.C. Chen “Applying the finite element method to drill design based on drill deformations”, Finite Element in Analysis and Design (1997).
36. “J. Audy, “A study of computer-assisted analysis of effects of drill geometry and surface coating on forces and power in drilling” (2008).
37. R.H. Thornley, A.B.I.El Wahab, J.D. Maiden, “Some aspects of twist drill design” (1987).
38. K. Narasimha, M.O.M.Osman, S. Chandrashekar, J.Frazao, “An investigation into the influence of helix angle on the torque-thrust coupling effect in twist drills”(1987).
39. M. Field, N. Zlatin, R.T. Jameson, “Machining difficult materials RENE 41, Metal progress” (1964).
40. J. Mazoff, http://www.mmsonline.com/article.aspx?id=14722; (2004).
41. J. Chae, “Investigation of micro-cutting operations” (2006).
42. X. Liu, R.E. Devor, S.G Kapoor, K.F. Ehmann, “The mechanics of machining at the micro-scale": Assessment of the current state of the science(2004).
43. D.A. Lucca, R.L. Rhorer, R. Komanduri, “Energy dissipation in the ultraprecision machining of copper” (1991).
44. J.D. Kim, D.S. Kim, “Theoretical analysis of micro-cutting characteristics in ultra-precision machining”(1995).
45.T. Inamura, N. Takezawa, Y. Kumaki, “Mechanics and energy dissipation in nanoscale cutting” (1993).
46. L.A. Kudla, “Deformations and strength of miniature drills, Proceedings of the institution of mechanical engineers” (2006).
47. L.A. Kudla, “Prevention against breakage of miniature drills” (2005).
48. J. Kaminski, R. Crafoord, “Positional accuracy of holes when drilling in inclined workpiece surfaces part I: experimental results” (1994).
49. Y. Gong “Dynamics of initial penetration in drilling: part I – Mechanistic model for dynamic forces” (2005).
50. J.C.J. Oxford, “Drilling, tapping and end milling of high strength materials”, engineering proceedings (1965).
51. Z. Yang, Q. Tan, E. Shiju, “Online monitoring of drilling torques of microdrills proceedings of the institution of mechanical engineers”(2004).
52. K. Iwata, “Basic study of high speed micro deep drilling” (1981).

53. R. Aronson, “making tiny holes, manufacturing engineering”(1996).
54. K. Lee, D.A. Dornfeld, “Micro-burr formation and minimization through process control”, precision engineering(2005).
55. L. Kudla, “Influence of feed motion features on small holes drilling process”(2001).
56. C.T. Sims, W.C. Hagel, “The superalloys”, Wiley, New York (1972).
57. E.A. Ezugwu, “high-speed machining of aero-engine alloys” (2004).
58. N. Narutaki, Y. Yamane, K. Hayashi, T. Kitagawa, K. Uehara, “high-speed machining of Inconel 718 with ceramic tools” (1993).
59. A. Devillez, F. Schneider, S. Dominiak. D. Dudzinski, D. Larrouquere “Cutting forces and wear in dry machining of Inconel 718 with coated carbide tools, wear” (2007).
60. P.K. Wright, G.J. Chow, “Deformation characteristics of nickel alloys during machining” (1982).
61. F. Klocke, G. Eisenblatter, “Dry cutting Manufacturing technology”(1997).
62. X. Yang, H. Kumehara, W. Zhang, “Experimental study for cutting performance of Ti(l-x)AlxN coated drills”, key engineering materials(2008).
63. Y.C. Chen, “Study on wear mechanisms in the drilling of Inconel 718 superalloy”(2003).
64. E.O. Ezugwu, Z.M.Wang, A.R. Machado, “Machinability of nickel-based alloys: A review” (1999).
65. B.M. Kramer, “Requirements for wear-resistant coatings, Thin Solid Films”(1983).
66. M.M. Donald, D.T. Quinto, “Twenty-five years of PVD coatings at the cutting edge, Society of vacuum coaters”- 50th Annual Technical conference proceedings (2007).
67. M. Hokka, D. Gomon, A. Shrot, T. Leemet, M. Baker, “Dynamic behaviour and high-speed machining of Ti-6246 and alloy 625 superalloys: Experimental and modelling Approaches” (2013).
68. Hongyanshi, Hui Li and ShengZhi Chen, “Temperature simulation and its application in on-line temperature measurement of micro drill bit” (2014).
69. Jung Soo Nam, Dae Hoon Kim, Haseung Chung, Sang Won Lee, “Optimization of environmentally benign micro drilling process with nanofluid minimum quantity lubrication using response surface methodology and genetic algorithm” (2015).
70. Rahamathullah and MS Shunmugam, “Thrust and torque analyses for different strategies adapted in Micro-drilling of glass-fibre-reinforced plastic”.

71. M. Imran, P. T. Mativenga, S. Kannan and D. Novovic, “An experimental investigation of deep hole micro drilling capability for a nickel-based super alloy”.
72. Philip A. Primeaux, Bin Zhang and W. J. Meng, “Performance of micro-drilling of hard Ni-alloys using coated and uncoated WC/Co bits” (2019).
73. A. Thakur, S. Gangopadhyay, K.P. Maity, “Effect of cutting speed and tool coating on machined surface integrity of Ni-based super alloy”, Procedia CIRP 14 (2014) 541-545.
74. A. Thakur, A. Mohanty, S. Gangopadhay, “Comparative study of surface integrity aspects of Incoloy 825 during machining with uncoated and CVD multilayer coated inserts” , Applied Surface science 320(2014) 829-837.
75. Yen, Y.-C; Sohner, J.; Lilly; B.; Altan, T., “Estimation of tool wear in orthogonal cutting using the finite element analysis”, Journal of materials processing technology (2004).